Dynamical Imaging of Surface Photo-potentials in Hybrid Lead Iodide Perovskite Films under High Optical Irradiance and the Role of Selective Contacts

*Silvia Maria Pietralunga**

Dr. Silvia Maria Pietralunga, Dr. Gabriele Irde, Dr. Alex J Barker, Dr. James M. Ball, Dr. Annamaria Petrozza, Dr. Vittorio Sala, Prof. Maurizio Zani, Prof. Guglielmo Lanzani, Prof. Alberto Tagliaferri

* *corresponding author*
Istituto di Fotonica e Nanotecnologie (IFN), CNR, Piazza Leonardo da Vinci 32, Milano, Italy
CNST@PoliMi, Istituto Italiano di Tecnologia (IIT), Via Giovanni Pascoli 70/3, Milano, Italy
E-mail: silvia.pietralunga@ifn.cnr.it

Dr. Gabriele Irde
CNST@PoliMi, Istituto Italiano di Tecnologia (IIT), Via Giovanni Pascoli 70/3, Milano, Italy
Dipartimento di Fisica, Politecnico di Milano, Piazza Leonardo da Vinci 32, Milano, Italy

Dr. Alex J Barker,
CNST@PoliMi, Istituto Italiano di Tecnologia (IIT), Via Giovanni Pascoli 70/3, Milano, Italy

Dr.James M. Ball,
CNST@PoliMi, Istituto Italiano di Tecnologia (IIT), Via Giovanni Pascoli 70/3, Milano, Italy

Dr. Annamaria Petrozza
CNST@PoliMi, Istituto Italiano di Tecnologia (IIT), Via Giovanni Pascoli 70/3, Milano, Italy

Dr. Vittorio Sala
CNST@PoliMi, Istituto Italiano di Tecnologia (IIT), Via Giovanni Pascoli 70/3, Milano, Italy
Dipartimento di Fisica, Politecnico di Milano, Piazza Leonardo da Vinci 32, Milano, Italy

Maurizio Zani
Dipartimento di Fisica, Politecnico di Milano, Piazza Leonardo da Vinci 32, Milano, Italy

Prof. Guglielmo Lanzani
CNST@PoliMi, Istituto Italiano di Tecnologia (IIT), Via Giovanni Pascoli 70/3, Milano, Italy
Dipartimento di Fisica, Politecnico di Milano, Piazza Leonardo da Vinci 32, Milano, Italy

Prof. Alberto Tagliaferri
CNST@PoliMi, Istituto Italiano di Tecnologia (IIT), Via Giovanni Pascoli 70/3, Milano, Italy
Dipartimento di Fisica, Politecnico di Milano, Piazza Leonardo da Vinci 32, Milano, Italy

Keywords: Hybrid lead-halide perovskites, High optical irradiance, Concentrated photovoltaics, Surface polarization, Time-Resolved SEM

To leverage the outstanding photonic qualities of lead halide hybrid perovskites for photonic applications under high optical irradiance, their reliability and temporal stability must be assessed. By performing Time-Resolved Scanning Electron Microscopy, it is found that when the free surface of MAPbI3 films is illuminated at 500 suns in vacuum, a giant photo-potential locally develops in tens of seconds and evolves differently depending on the charge-selective film substrate. It is reversible on timescales of minutes in the case of hole-transporting PEDOT:PSS, while more persistent effects occurs, on the timescale of hours, in the case of electron-transporting TiO2. In addition,films grown on TiO2 show an irreversible decay of photoluminescence intensity measured in-situ at same conditions and photoinduced alteration of the work function at some grain boundaries. Different response at high irradiance in the two systems can be due by contact-dependent and light-induced spatial redistribution of charged defects, either ions or localized dipoles. It is also clear that photoexcited electrons and holes play different roles in the photochemistry of the systems depending on selective contacts, and are likely to mediate diverse photo-assisted redox reaction paths. The TiO2 layer may also act as a photocatalyst, leading to MAPbI3 degradation and to irreversible polarization, which would hinder high-irradiance applications.

1. Introduction

Methylammonium lead halide perovskite thin films are best performing emerging photovoltaic (PV) materials, with certified record values for Power Conversion Efficiency higher than 25% [1–5]. An enormous amount of scientific investigation has been devoted to unveil the secrets behind their success and to solve the issues still preventing their commercial leverage on a large scale. The peculiar qualities of halide perovskites would also appeal to exploitation in High-Concentration Photovoltaic systems [6–8] up to irradiance levels equivalent to hundreds of suns (1 sun sunlight standard irradiation being 100mW/cm^2, at AM 1.5 G), as well as in light sources and lasers [9–13]. Both fields of application share high levels of optical irradiance and

free charge density under operating conditions, which represent open challenges to achieve high performances [14–16]. Recently published works describe irreversible degradation of perovskite films illuminated at high optical irradiances [17–19]. Specific examples of light-activated perovskite decomposition are reported, the amount of which depends on conditions of irradiation, as well as on composition and on operating temperature. High charge injection regimes are likely to emphasize issues related to the photogeneration of local space charge domains [20,21]. More in general, the photophysics and the optoelectronic response of hybrid perovskites under strong excitation regimes still represent open fields of investigation.

Surface photo-potential, or *surface photovoltage* (SPV), contributes to unveil the photophysics of systems, by probing the variations in the electrical potential and work function at the sample surface under illumination with respect to dark conditions, as can be originated by charge redistribution [22].

In solar cells under operating conditions, SPV values correspond to the open-circuit voltage V_{oc} at the illuminated side [23]. In assessing V_{oc}, selective charge transport layers and their interfaces with the perovskite absorbers play a crucial role, the physical–chemical origin of which is still the object of scientific debate [24]. Precious information regarding charge transport dynamics, internal electric field configurations and interface energetics of perovskite films under illumination can also be retrieved by probing SPV directly at film free surface. Photo-assisted Kelvin probe (KP) contact potential [23–25] has been used to investigate the buildup and decay over seconds of the energy levels at device surface and interlayers [24,25], In steady state, the distribution of space charge fields, photo-generated across the device sections have been identified using KP microscopy [26] and the dependence of SPV on selective charge transport layers in perovskite films and solar cells was assessed by KP spectroscopy [27]. The investigations reported up to now did not address high optical irradiance conditions and were not devised to provide dynamical mapping of surface photo-potentials.

In this work we apply the technique of Laser-assisted Time-Resolved Scanning Electron Microscopy (TR-SEM) to provide the dynamical imaging of SPV, as induced by optical irradiance up to 500 suns in Methylammonium lead iodide ($MAPbI_3$) films deposited on two diverse charge extracting substrates, namely a hole transport layer (HTL) of poly (3,4-ethylenedioxythiophene) polystyrene sulfonate (PEDOT:PSS) and an electron transport layer (ETL) of compact TiO_2. TR-SEM was recently introduced as a new and fast way to visualize photoinduced polarization at high irradiances [28]. It is based on the assumption that spatial modulations in work function can be depicted as secondary electron (SE) contrast patterns [29]. These can be originated by photoexciting excess charge carrier distributions in the subsurface volume [30,31], as well as by changing the configuration of surface dipoles or by optically activating redox reactions at a local level. The advantage of TR-SEM in probing SPV is that it combines surface mapping over a broad range of possible view fields, with nanoscopic depth selectivity and spatial lateral resolution. TR-SEM is capable of real-time imaging from the millisecond regime (compatible with raster scanning frequency) to the quasi-steady-state. Therefore it can investigate optically excited phenomena evolving on a wide range of timescales. The ultrafast temporal regime can be reached by laser-driven dynamical SEM configurations based on pulsed electron beams and operated in pump-probe mode [32,33].

For the present investigation,the TR-SEM apparatus has been complemented with a correlative setup for *in-situ* measurement of quasi-steady-state Photoluminescence (PL) in the same conditions of TR-SEM, giving access to information from the surface (TR-SEM, < 1 nm) and the bulk (PL, ~ 100 nm) of the same spot.

TR-SEM shows that by illuminating the free surface of $MAPbI_3$ films at 500 suns, a giant photo-potential in the volt range locally develops in tens of seconds and evolves differently depending on the nature of charge-selective film substrate. The different dynamics observed on the $MAPbI_3$/PEDOT:PSS heterostructure (hereafter labelled as MAPI/P) with respect to the $MAPbI_3/TiO_2$ heterostructure (labelled as MAPI/T) unveil a major influence of the interfaces

and the diverse roles played by electrons and holes in $MAPbI_3$ photochemistry. While the effects measured in MAPI/P are reversible over timescales of minutes, the photo-polarization at surface of MAPI/T) is semi-permanent over timescales of hours. As detailed in the next section, being SEM imaging extremely sensitive to surface, optically induced irreversible damaging is reasonably excluded in MAPI/P. On the contrary, the long-lasting surface polarization effects in MAPI/T are compatible with a certain degree of permanent degradation of the material. SEM images of MAPI/T surface at sub-micron scale suggest that very long-lasting modifications in the work function occur at the grain level. The effects are compatible with the photo-generation of local charge fields, but other possible causes of damage cannot be a-priori excluded in the present context.

The measured decay of PL intensity over time is consistent with the hypothesis that non-radiative and defect-mediated charge recombination is optically activated [34–36]. In MAPI/P, PL decays faster than in MAPI/T, and MAPI/P photoexcitation is partially reversible after resting the film in the dark. On the contrary reversibility is absent in the case of MAPI/T. The results are discussed in the hypothesis that different types of photogenerated charge traps are activated by high optical irradiance in either systems. In addition, the TiO_2 layer may act as a photocatalyst of chemical reactions leading to degradation of the perovskites and to a permanent polarization of the film.

1. Experimental and Results

2.1 $MaPbI_3$ films

$MAPbI_3$ thin films of comparable thickness (270-300 nm) have been synthesized according to the *two-step interdiffusion* method [37] on PEDOT:PSS and TiO_2 substrates as MAPI/P and MAPI/T structures (details are provided as *Supporting Information*). They represent incomplete configurations of solar cells, of an *inverted p-i-n* structure (MAPI/P) and of a *standard n-i-p* structure (MAPI/T) [1] respectively, with the free surface of the $MAPbI_3$ film exposed. High

resolution SEM images of the film surfaces and cross-sectional schemes of the structures are shown in **Figure 1.** Films are equivalent in structure [38], with average dimensions of the grains being slightly larger in the MAPI/T case. Since SEM views have been taken in totally equivalent measurement conditions, the higher brightness of MAPI/P surface indicates a more efficient Secondary Electron (SE) emission.

2.2 Setup for TR-SEM and in-situ PL

The working principle of TR-SEM was recently introduced [28]. A customized commercial SEM (Mod. Tescan MIRA III) is provided with optical viewports to focus light into the chamber and to illuminate the surface of the sample being tested. In ordinary SEMs image contrast is contributed by sample morphology and by work function local differences [39,40]. In TR-SEM, under illumination, photo-assisted chemical reactions and phase transformations as well as photoexcited electrical fields modify the work function of the material, leading to detectable contrast patterns. By acquiring real-time SEM images during illumination and after it, dynamical maps of photoinduced patterns are obtained.

In this work, a setup for *in-situ* PL characterization has been introduced in the TR-SEM setup. The experimental apparatus is pictured in **Figure 2(a),** showing the measurement chamber with the SEM column and the in-chamber termination of the optical feedthrough to collect the PL signal. The corresponding scheme is drawn in **Figure 2(b).** A CW (continuous wave) diode laser emits deep blue light at λ = 405 nm (3.06 eV), that enters the chamber and is focused at grazing incidence on the sample surface to provide optical excitation at intensities 1.5 – 50 Wcm^{-2}, equivalent to 15 – 500 suns. Optically induced morphological damage is avoided by keeping the exciting optical intensity far below an ascertained threshold (500 W cm^{-2}) [41]. Care was also taken to minimize electron-beam damaging of the $MAPbI_3$ films [28]. Under SEM operating conditions the perturbation induced in the material by the Primary Electron (PE)

beam is negligible with respect to optically induced effects, in terms of energy deposited over the excitation volume and of excited excess charge carrier density.

Tilting of the samples at $\theta = 45°$ provides a configurational asymmetry which conveys the information on photoexcited electrical phenomena. The photo-generated charge carriers drift-diffuse inside the MAPI along the normal to the sample top surface, resulting in localized surface charge distributions and voltage difference between the bulk of the material (at ground potential) and the illuminated area at surface. The local surface fields couple with the detection geometry to produce TR-SEM bright-dark contrast patterns, shown in panel (a) of **Figure 3**, encoding the information on the sign, the density and distribution of the local photogenerated charges. [28] More details on the TR-SEM apparatus, on the role of asymmetric samples and of numerical modelling are reported as *Supporting Information*.

2.3 TR-SEM dynamical imaging

Results of surface dynamics shown by TR-SEM are illustrated in Figure 3, with the first and second rows referring to MAPI/P and MAPI/T respectively. Figure 3(a) shows images in *Laser ON* conditions, taken after CW illuminating the film for 120s, and in *Laser OFF* conditions, taken after resting samples in the dark for 120s. The dotted ellipse highlights the laser spot. The asymmetric bright-dark contrast that develops across the illuminated region is caused by the $\theta = 45°$ tilt of the samples and is related to localized voltage distribution, (see **Figure S1** in *Supporting Information* for further details, as well as **Figure S2** and **Figure S3** for complete temporal sequences of photoinduced TR-SEM contrast maps taken in both samples). The upper part of the frames pictures a region of the tilted sample which is closer to the SEM column along its axis.

Figure 3(b) shows cross-sectional contrast profiles extracted from series of images (not shown, see Figures S2 and S3) acquired at subsequent times, to better appreciate the temporal evolution of TR-SEM contrast. Figure 3(c) plots peak-to-peak values of the contrast amplitude profiles.

Let us discuss TR-SEM patterns induced in either sample. On MAPI/P under illumination the photoinduced contrast is weakly negative when averaged over the spot area, indicating a reduction in SE collection from the illuminated area, and a faint bright-to-dark transition is visible along the minor axis of the ellipse. On turning off illumination the average photoinduced contrast turns positive, and the orientation of the bright-to-dark transition is reversed. The case of MAPI/T is different, in that under illumination the average photoinduced contrast is negligible, although a sharp dark-to-bright dipolar contrast pattern is present, oriented opposite to that in the MAPI/P case. On switching off the illumination, the average photoinduced contrast remains negligible, and the dark-to-bright dipolar contrast shows no sign inversion, its amplitude decreasing slightly, which leads to a final situation qualitatively similar to the case of MAPI/P. More details can be gleaned by analyzing the sequence of contrast profiles in Figure 3(b). In MAPI/P on turning on the light, the signal amplitude quickly increases within a few seconds, and substantially saturates within 120s. As light is switched off, contrast reversal occurs within one second, the observation of the switching rate being limited by the sampling rate. Then a very slow decay of the signal occurs in the dark over 180s, as also confirmed by the peak-to-peak evolution. In the case of MAPI/T, under illumination the signal profile is mirrored about the horizontal axis with respect to that of MAPI/P. The signal amplitude reaches its maximum on switching light on and then it steadily decreases. On switching light off, the contrast amplitude is slightly reduced within one second without inverting sign and then it resumes its decreasing trend. Experimental results in TR-SEM are supported by a numerical simulation of the process of SE detection in the presence of localized voltage distributions at

sample surface [28] (see also *Supporting Information*). Examples of experimental and simulated cross-sectional contrast profiles are shown in **Figure 4.** A selection of profiles from Figure 3, measured on MAPI/P and MAPI/T respectively in L*aser ON* and *Laser OFF* conditions, shown in Figure 4(a), is compared to calculated SE collection profiles, in Figure 4(b), as originated from normal distributions of positive and negative surface potentials (dashed lines). From comparison it is clear that TR-SEM contrast profiles recorded on MAPI/T match the occurrence of a positive SPV. On the contrary, in the case of MAPI/P contrast profiles recorded under illumination correspond to a negative SPV distribution, which eventually switches to positive as light is turned off. We have previously discussed [28] that an agreement in functional shape between simulated and experimental TR-SEM profiles in $MAPbI_3$ films under high irradiance conditions is obtained at values $V_{pk} > V_{bi}$, where $V_{bi} = 0.7 - 1.1\,V$ [25,42] is the built-in voltage. Presently simulated profiles correspond to $V_{pk} = \pm 5\,V$. The excitation of higher SPV than V_{bi} is the fingerprint of an electrostatic contribution added as the result of optically induced polarization [23].

One additional striking feature in Figure 3(a) is the appearance of a contrast pattern extending beyond the illuminated area. The pattern is very pronounced in MAPI/T, while in MAPI/P it is merely perceivable and more localized. Temporal series of cross-section profiles in Figure 3(b) and of contrast patterns (in Figures S2 and S3 in *SI*) reveal that in MAPI/T the lateral pattern substantially builds up within some 30 s after starting illumination (*Laser ON*) and negligibly decays over the first 3 minutes in the dark *(Laser OFF)*, substantially sharing the dynamics of the positive SPV distribution. On the other hand, in MAPI/P it is absent in *Laser ON* condition, it builds up within one second from turning the *Laser OFF* (limited by scan rate) and decays quickly over the first 3 minutes.

The reversibility of the photo-generated voltages is radically different in MAPI/P and in

MAPI/T. In Figure 3(c) , a decay trend of TR-SEM peak-to-peak contrast amplitude in dark conditions is evident for MAPI/P. In MAPI/P, the long-term evolution of the peak-to-peak and of the average TR-SEM contrast in the dark was characterized previously and the reversibility of the photo-generated charge distributions was assessed at several values of optical irradiance [28], showing that higher optical fluence corresponds to longer-living contrast (see also Figure S5 in *Supporting Information*). By interpreting it as originating from a photo-potential, it can be stated that SPV excited in MAPI/P at high optical irradiance is ultimately a fully reversible phenomenon. On the contrary, in case of MAPI/T, the decrease of contrast in the dark saturates to finite values over timescales of hours (see **Figure S6**). The persistence in time of light-induced modifications on MAPI/T was also documented by top-view high-resolution SEM images in **Figure 5**(a-d). The reference image of the surface prior to illumination (a) is compared to image taken after irradiating the sample at 500 suns for 480 s and keeping it in the dark for 10 min (b). A pixel-by-pixel subtraction with the reference image issues a 2D differential contrast plot (c) that highlights the illumination-induced modifications. At odds with findings by Li et al., that irradiated samples at 7 suns in UHV environment [17], in the present case there is no evidence of a morphological alteration at the microscale. However, a darker photoinduced contrast is noticeable on selected grain surfaces, highlighted by white contours in Figure 5, which indicates slowly evolving and semi-permanent phenomena locally affecting the work function.

2.4 In –situ Photoluminescence

Equivalent conditions of illumination of TR-SEM were used to excite *in-situ* quasi–steady state PL.

The results of quasi-steady state PL characterization on both systems, illuminated at 500 suns and at 15 suns are shown in **Figure 6** and are characterized by a PL intensity decay (PLID) of the spectrally integrated signal.

The evolution of PLID has been fitted by stretched exponential functions of the kind $I(t) = I_0 exp\left[-(t/\tau_c)^{\beta}\right]$, where τ_c is a reference decay time and the stretching exponent $0 \leq \beta \leq 1$ expresses the heterogeneity of the system [43,44] (more heterogeneous at lower values). An average decay time $< \tau >$ can be defined as $< \tau >= \frac{\tau_c}{\beta}\Gamma\left(\frac{1}{\beta}\right)$ for the ensemble of the trapping configurations, where Γ is the gamma function [45,46]. $< \tau >$ is the inverse of the time-averaged decay rate constant and here represents an effective depletion time for luminescent upper levels. The fitting parameters are collected in Table 1.

Under illumination at 500 suns both samples evolve similarly with minor differences, being MAPI/T slightly slower, and the decay proceeds rapidly in the first few seconds until it saturates at about 10% of the initial signal value within some tens of seconds. At 15 suns, PLID in MAPI/P is similar to the higher irradiance case and saturates in less than 150 s. In MAPI/T it is much slower and does not saturate within the temporal span of the test.

Higher β values ($\beta \to 1$) indicate the predominance of one specific quenching mechanism (mostly found in homogeneous systems), while lower values ($\beta \to 0$) indicate the presence of multiple coexisting de-excitation paths (often found in more heterogeneous systems) [47]. At 15 suns PLID in MAPI/T is considerably slower than in MAPI/P; $\beta \to 1$, so that a nearly unique de-excitation channel is likely active in both samples, although it is not necessarily the same channel. At 500 suns PLID accelerates and proceeds with comparable time constants in both systems, presenting lower β values that suggest an increased heterogeneity in the population of PL quenching sites at higher irradiance.

Further insight is gained from the dynamics shown after a subsequent illumination period. In the case of MAPI/P, on turning illumination on again after keeping the samples in the dark for 2 minutes the PL signal partially recovers. The level attained is comparable at both irradiation levels and close to the unquenched PL value at 15 suns. Fitting of recovered PLID leads to the following quenching dynamics parameters: $\tau_c = 13.69s(13.74s)$, $\beta = 0.8\ (0.7)$ and $< \tau >=$

$15.81s (17.1s)$ respectively for the case at 15 (500) suns. Conversely, in MAPI/T no recovery of the PL occurs at either irradiation levels. Integrated PLID curves of Figure 6 are mainly contributed by the quenching of the band-to-band radiative recombination PL peak at 772 ± 2 nm [42] (spectrum not shown here, see Figure S6 and Figure S7 in *Supporting Information*.). At 500 suns, further spectral features in PL appear, which might be related to some kind of photoinduced lattice instabilities and photo-chemical modifications [48–50].

3. Discussion

3.1 Influence of the transport layer on the dynamics at $MaPbI_3$ interfaces.

The different brightness of SEM images for MAPI/T and MAPI/P in Figure 1 shows that charge selective contacts affect the free charge transport dynamics. The role played by each transport layer is discussed with reference to **Figure 7** and involves both the interface with the substrate and the free film surface During SEM operation, the net electronic excess charge population that is injected by the electron beam is small, so that quasi-equilibrium conditions apply[10,39] and a unique Fermi energy level $E_{F,T} = E_{F,MAPI} = E_F$ and $E_{F,P} = E_{F,MAPI} = E_F$ establishes across the MAPI/T and MAPI/P structures, respectively, $E_{F,T}$ is the Fermi level for the TiO_2 contact layer, $E_{F,P}$ for the PEDOT:PSS contact layer and $E_{F,MAPI}$ for the $MAPbI_3$ layer. Let $\Phi_{MAPI}(z) = E_{vac} - E_{F,MAPI}$ and $\Phi_T(z) = E_{vac} - E_{F,T}$ and $\Phi_P(z) = E_{vac} - E_{F,P}$ be the depth dependent work functions inside the three layers. The condition $\Phi_T < \Phi_{MAPI}$ in MAPI/T [15,24,52,53] leads to a downward bending of the energy bands at the $MAPbI_3$ to TiO_2 heterojunction, which facilitates free electrons extraction at the ETL contact [24] and drains the small excess electron current which is injected during SEM imaging. The opposite condition $\Phi_P > \Phi_{MAPI}$ applies in MAPI/P [53], leading to the building up of an energy barrier at the $MAPbI_3$ to PEDOT:PSS junction which limits electron extraction at the HTL contact and favor negative charge accumulation in the film under SEM operation. This contributes to increased

SE emission and brighter images [40].

In line with reported cases in inorganic semiconductors [39,40], the second contribution leading to different SEM image brightness in the two samples is the pinning of the Fermi level at the $MAPbI_3$ free surface, which cannot be excluded *a-priori* and may indicate unequal doping of $MAPbI_3$ films. Though generally considered as a quasi-intrinsic semiconductor featuring ambipolar charge transport [1,3,14], the soft crystalline structure of $MAPbI_3$ hosts a wide variety of intrinsic defects resulting in substrate-dependent unintentional *p*-type or *n*-type self-doping [21,53–58]. Specifically, $MAPbI_3$ generally grows *p*-type on PEDOT:PSS [24,59,60], whilst both *p*-type and *n*-type cases are reported in case of TiO_2 substrate [53,61,62]. The free surface of a semiconducting film may be considered a 2D semiconductor itself, in equilibrium with its bulk and sharing the common Fermi energy level $E_F = E_{F,S}$, where $E_{F,S}$ is the Fermi level at surface [63]. The distribution of the density of states at the surface can *pin* $E_{F,S}$ to a specific intragap energy level, so that $\Phi_S = E_{vac} - E_{F,S}$. In case $\Phi_{MAPI} < \Phi_S$ $(\Phi_{MAPI} > \Phi_S)$, the energy bands of the $MAPbI_3$ at surface are bent upwards (downwards). Energy band bending at the surface of polycrystalline $MAPbI_3$ films has been addressed by several authors [62,64–66] and De Bastiani *et al.* and Yuan *et al.* have highlighted how the configuration of defects at surface, interfaces and grain boundaries (GBs) crucially depends on film growth and operating conditions in a complex and fairly unpredictable way [41,67]. In the present case, we suggest a slightly *n*-type character for the $MAPbI_3$ film in MAPI/T resulting in upward surface band bending [62] acting as a voltage barrier to SE emission, as plotted in Figure 7. For MAPI/P, a slight *p*-type doping is suggested, leading to downward band bending at the free surface, which instead favors SE emission by providing an accelerating field. Thus, both the doping nature and the type of surface band bending can contribute to MAPI/P being brighter than MAPI/T in SEM images (as shown in Figure 1).

3.2 Dynamics under high irradiance.

The dynamics of the illuminated region in the two systems under CW high irradiance conditions is sketched **Figure 8** (a,b,d,e). In $MAPbI_3$, with an optical bandgap at $E_g \cong 1.6$ eV and an absorption length in the blue of $\sim 140nm$ [28], about 85 - 90 % of the light entering the film is absorbed over its thickness, while a non-negligible fraction (10-15%) reaches the selective contact layer at the bottom.

Differently developing TR-SEM contrast dynamics on MAPI/P and on MAPI/T can be explained by considering the concomitance of three combined photoinduced contributions to SPV. These are: optically induced energy band flattening at surface, free charge unbalance and the segregation of charged defects resulting in the creation of a macroscopic polarization across the illuminated $MAPbI_3$ film. Band flattening (in Figure 8(a)) occurs as a consequence of the optical excitation of a dense plasma of free *e-h* pairs at the subsurface volume. In the present case, strongly absorbed intense blue light is estimated to generate an excess carrier density $\Delta n, \Delta p \sim 10^{17} \div 10^{18} \mathrm{cm}^{-3}$ within few 10 nm below the surface [26]. Such a carrier density is actually comparable to bleaching conditions for optical transparency in perovskites [68] and to the threshold injection density for light amplification and lasing [12,16]. By exceeding the degeneracy level, estimated at $n_c = 5 \times 10^{16} cm^{-3}$ for $MAPbI_3$ [14,69], it locally drives the subsurface volume into conduction. The out-of-equilibrium condition leads to temporary unpinning of the Fermi level at surface and to energy band flattening [22] by an amount $\Delta\Phi_s = \Phi_s - \Phi_{MAPI} = -eV_{pv}$ where e is the unitary charge and V_{pv} is the free-carrier induced SPV. The amplitude V_{pv} is a function of the doping level and of the energy of the surface states that pins the Fermi level and is typically in the range $qV_{pv} = E_g/2 \div E_g$ [22]. In MAPI/T, band flattening acts in strongly reducing the energy barrier that opposes to SE emission, so that illuminated regions may look brighter than non-illuminated ones. On the contrary, in MAPI/P films it removes the accelerating field which favors SE emission, so that illuminated regions

may look darker. This explains both the average darkening in the illuminated region of MAPI/P and the slightly increased average brightness on MAPI/T in *Laser ON* conditions, shown in Figure 3. Therefore TR-SEM analysis at the free surface of $MAPbI_3$ highlights differences in the bulk and surface energetics of films, grown by a nominally identical procedure on different substrates.

Besides band flattening, the TR-SEM contrast patterns measured in *Laser ON* condition also reveal the building up of a SPV which is positive in MAPI/T and negative in MAPI/P, as shown in Figure 4. We explain this finding by the formation of a photo-generated bipolar net charge distribution across the film thickness, which is of opposite sign in MAPI/T and MAPI/P as the result of the major role played by the ETL and HTL charge selective contacts, as sketched in Figure 8 (b,d). The *n-i* MAPI/T and *p-i* MAPI/P stacks are two open-circuited diode structures, with the $MAPbI_3$ film playing the role of the photoanode and photocathode, respectively. Over time, a dynamical equilibrium condition is reached in the illuminated region, characterized by a free charge imbalance in the film volume. MAPI/T transfers electrons at the TiO_2 interface, leaving the film subsurface more positively charged, while MAPI/P transfers holes at the junction with PEDOT:PSS, issuing an uncompensated excess electron density at the subsurface. A population of intragap deep electron traps are photo-generated in $MAPbI_3$, following the strong illumination gradient, and filled by photoexcited electrons. The resulting surface charge unbalance between the illuminated region and the surroundings is illustrated in the annex to Figure 8 (red framed). The formation of bright-dark TR-SEM contrast patterns are consequence to this process (see also Figure S2 in *Supporting Information*).

The phenomena described so far are related to free-charge excitation and diffusion in the subsurface volume, "instantaneously" with respect to minimum timescale of observation (seconds). As observed earlier, the effects of intense illumination on $MAPbI_3$ films also involves dynamics on the longer timescale. The experimental contrast profiles in Figure 3 evolve over tens of seconds, that is a typical signature of light-activated ionic

motion [20,21,23,65,70] and of the evolution of charged polar defects [34,49,50,69,71,72]. Illumination intrinsically boosts ionic conductivity by promoting photo-generated defects and by reducing their activation energy [50]. In the presence of strong optical absorption gradients, ionic defects migrate as a combined drift-diffusion process mediated by the strong density gradient of mobile and ionized point defects and also by the free-carrier photovoltage V_{pv} [64,65,67,73,74]. In 300nm-thick films, values as low as $V_{pv}{\sim}0{,}3V$ actually behave as an intense self-biasing, equivalent in magnitude to external poling and large enough to drive ionic drift and segregation of chemical species along GBs and at the surface [17,65]. So, we consider that dynamical TR-SEM surface patterns may be originated by temporally evolving defect-related space charge fields [64,65,75]. DeQuilettes and co-workers [21] demonstrated experimentally that, in a case similar to ours of unbiased films under vacuum conditions, negative iodide species (e.g. interstitial I^- ions) migrate away from the illuminated free surface and pile up at the back interface. Positive charge accumulation at the subsurface volume include residual vacancies V_I^+ [58,76], but may also involve MA^+ and even lead-related defects such as Pb^{2+} and others [21,59,77], activated under present condition of high optical irradiance and contributing to material polarization [3,34,78]. Such a possibility was theoretically calculated by Azpiroz et al. [79] and experimentally demonstrated by Xing et al. [50]. Surface enrichment in positive charges may also come from photo-assisted dissociation of $MAPbI_3$ followed by removal of volatile species in vacuum [17,80]. Since many of those defect centers possess a donor-like character, their formation has been also revealed in terms of local *n*-type photo-doping of the film surface [62,65,81]. The photo-generation molecular polar domains [49,70,82] is one further possible source of local surface polarization. The nature and density of these optically-induced point defects are composition-dependent and not fully controllable [83]. Many of them also contribute localized metastable deep trap states for electrons [34,49,84]. The accumulation of electrostatic space charge may result actually in the buildup of a surface photo-potential higher than that

contributed solely by the band-flattening effect [23]. High densities of light-excited uncompensated defects of the order of $N \sim 10^{19} cm^{-3}$ accumulated over tens of nanometers in thickness (w) may express surface voltages over the range $V_{pv} = \frac{qNw^2}{2\varepsilon_0\varepsilon_r} = 0.1 - 10$ V [3,78]. This supports results in Figure 4, indicating that SPV in the volt range are optically excited. So, in *Laser ON*, concomitant conditions of high optical irradiance and strong density of photoinduced excess free charges may trigger quite complex and competing charge transport mechanisms, resulting in measured SPV.

Figure 8 (b,d) provides a schematic representation of concurrent possible space charge phenomena occurring under high CW irradiance and which finally express a net sign for SPV in the illuminated region.

Also the formation of the photoinduced lateral contrast surface pattern, quite evident in MAPI/T (Figure 3(a)) may be ascribable to specific mechanisms of local space charge buildup in the polycrystalline film. The lateral optical intensity gradient of the focused optical beam may activate a diffusive ionic motion, also extending laterally beyond the illuminated area. Ions move more preferably along GBs and interfaces [47,50,85,86] since their motion is defect-mediated. Patterns can be the results of the photo-activated concentration of space charge fields at specific locations and GB, confirming the key role played by GB in the photochemistry of $MAPbI_3$ [3,36,87].

The picture drawn above on the basis of TR-SEM, on the trapping kinetics in $MAPbI_3$ and its dependence on photoexcitation intensity [3,36], is supported by the direct measurement of radiative recombination provided by PL measurements. Time-resolved PL is complementary to TR-SEM in two main aspects: the PL signal is originated throughout the whole thickness of the films (~300 nm), opposite to TR-SEM that is extremely surface sensitive, and it is not influenced by the presence of fields, including the one associated with SPV. As a consequence the decay of PL intensity, PLID, is a metric of the timescales of photoinduced transformations

in the bulk of neat $MAPbI_3$ films, leading to a decrease in time of the probability of radiative de-excitation of the material. Several authors observed reversible PLID in $MAPbI_3$ at low irradiance levels and related it to the photoexcitation of metastable traps and non-radiative charge recombination sites, either associated to photoinduced dipolar structural modifications, or by ionic excited states [35,36,49,70,82,84,88]. Timescales of PLID shown in Figure 6 are consistent with the hypothesis of photoinduced defect formation and ion/defect migration and annihilation [35,50,78,82,89]. The heterogeneity of the non-radiative defects increases as a function of the irradiance in a similar way in MAPI/P and MAPI/T, as testified by the close values of the stretching parameter β obtained at 15 and 500 suns (Table 1). On the other hand, present PLID results show a different bulk behavior of MAPI/T and MAPI/P in *Laser* ON conditions, which couples with the different behavior observed at surface by TR-SEM. Slower dynamics in MAPI/T may originate from a less efficient activation of non-radiative defects, in connection to the larger dimension of grains in the polycrystalline film. A large average density of photogenerated defects, about $\sim 10^{19} \mathrm{cm}^{-3}$, may be formed by illuminating $MAPbI_3$ over hundreds of seconds [49,70,82], which is expected to be highly non-uniform with peak concentrations at surfaces and GBs. Therefore, lower interfaces-to-volume ratios, as in polycrystalline films with bigger grains, may decrease the generation rate of non-radiative recombination centers [35,50]. For both systems, PLID kinetics is faster at 500 suns than at 15 suns, indicating a higher density of non-radiative photogenerated defects, while their nature may vary locally and lead to different characteristic times. Saturation of PLID indicates a dynamical balance between trapping and detrapping mechanisms, combined with possible dynamics of photogeneration and light-induced curing of different populations of defects [35,90]. To summarize, under intense CW illumination TR-SEM contrast patterns unveils the build-up of a surface photo-potential contributed to by the interplay of plasma-induced band flattening, free charge accumulation in the subsurface volume and spatial segregation of charged defects. It is known that high excess density of photo-generated free charges may also mediate different

paths of photo-chemical redox reactions in various $MAPbI_3$ systems [35], which can be at the origin of different populations of defects We suggest that in the present case, the defect-related contributions to photoinduced polarization in MAPI/T and MAPI/P may be the cause of the different reversibility of the two systems.The difference is mostly evident in the dynamics of decay of SPV and PL in the dark, as described in the following.

3.3. Decay dynamics in dark conditions

As illumination is turned off, the band flattening and the free-charge contribution to surface polarization vanishes on sub-second timescales, ruled by dielectric relaxation, charge detrapping [36] and recombination rates [42], unshielding the photoexcited ionic charge field. TR-SEM shows that in both MAPI/T and MAPI/P, a positive space charge is left in the subsurface volume of the laser spot, and a negative charge in the volume close to the transport layer interface, resulting in positive SPV. We suggest that this configuration results from the migration of negative ions that took place during illumination. In MAPI/T the effect is visible as an added contribution, suddenly increasing the contrast amplitude, while in MAPI/P the sign of the TR-SEM contrast is rapidly switched, as is evident from the experimental images in Figure 3. This condition is sketched in Figure 8(c, f). Quasi-equilibrium recovery condition in the dark unveils the dipolar photoinduced ionic field, causing *n*-type doping in the subsurface volume and expressing a positive SPV to the pristine surface region of the film. The decay of the TR-SEM contrast in the dark is much slower than its buildup [28], as shown in Figure 3. Recovery times of minutes and hours are compatible with back-diffusion and drift of ions in the dark [21,26,49,50,77,78], combined with thermally driven de-excitation of charged metastable trap states and polar defects [49,69,84], finally leading to defect recombination [42]. Photo-polarization effects in perovskite systems, measured at irradiances up to one sun, are usually reversible [49,55,60,73,77,80,91], albeit non reversible light-induced degradation of the material is possible [92]. We show that, after illuminating the two systems at the same level of high

irradiance, their recovery kinetics strongly differs. In MAPI/T, surface photo-potential observed by TR-SEM persists on time scales of hours, and PLID does not recover after a 2 minutes dark period of the system. Moreover, in MAPI/T the generation of PL quenching sites seems also to proceed for a few minutes in the dark. A tentative mechanism compatible with this observation is that part of the photoexcited defects decay to metastable non PL-active sites. Opposite to MAPI/T, in MAPI/P surface photo-potentials are reversible on faster time scales and PL signal is restored by resting in dark. Since variations in local crystalline environments may lead to quite different dynamics probed on nominally equivalent samples and locations [62,88], PLID results also suggest that different sites are generated according to the different contact layers. We suggest that the different behavior of MAPI/T and MAPI/P is strongly influenced by different energetics and photo-chemistry at the substrate interface. Actually, charge selective contacts are known to crucially affect the whole structure of $MAPbI_3$ films, the concentration and type of defects at the junctions and the transport properties and performances in solar cells [60,65,93].

Also, the role of TiO_2 contact in favoring the formation of long-lasting space charge fields and related effects, in the case of the *standard* perovskite solar cell structure, has been widely assessed [67,82,94–99]. The TiO_2 substrate is even known to act as a photo-catalyst for the decomposition of the perovskite at a local level, giving rise to the production of volatile species like I_2, H^+ ions and methylamine molecule CH_3NH_2 [100]. We deem that such a process is likely to occur in vacuum, since oxygen and moisture are not essential ingredients to activate $MAPbI_3$ degradation. The positive polarization at surface contributed by photo-assisted dissociation of $MAPbI_3$ [17,80] is irreversible. In fact, local contrast variations at grain surfaces shown in Figure 5 suggest that in case of MAPI/T, photoinduced degradation may be activated at specific crystal grains, forming semi-permanent dipoles and space charge fields and preventing the complete recovery of pristine pre-illumination conditions. Also the absence of recovery of PL after resting in the dark confirm that MAPI/T is more prone to permanent modifications.

4. Conclusion

The photophysical evolution of $MAPbI_3$ films under high optical irradiance was characterized by a novel experimental setup combining Time-Resolved SEM and quasi steady-state *in-situ* PL characterization at comparable excitation conditions. The free surface of films has been illuminated by intense blue light, up to 500 equivalent suns, in vacuum conditions and without electrical biasing. Films were grown by the same two-step interdiffusion method on two different charge-selective substrate contacts, namely compact TiO_2 (ETL) and PEDOT:PSS (HTL), and named respectively MAPI/T and MAPI/P structures. TR-SEM and PL analysis at the free surface of $MAPbI_3$ highlights differences in the bulk and surface energetics of films, grown by a nominally identical procedure on different substrates.

Results show that the specific kind of substrate crucially affects the electrical and photoelectrical dynamics of illuminated films, as well as their recovery in the dark. Electron microscopy suggests that semiconducting $MAPbI_3$ grows more *p*-type on PEDOT:PSS than on TiO_2. Under intense illumination, TR-SEM probes a strong net photo-potential at the free film surface, which builds up in tens of seconds. This photo-potential is positive for MAPI/T and negative for MAPI/P. Different kinetics for PLID in the two systems, suggesting the substrates of MAPI/T and MAPI/P affect the formation of light-activated metastable defects, leading to different charge space unbalances and non-radiative recombination path for free carriers. In dark conditions after irradiation, both systems show a giant surface photo-potential of the order of volts, which in this case has the same positive sign and is tentatively attributed to the accumulation of uncompensated positively charged defects in the subsurface volume. Slow recovery dynamics are observed in the dark, compatible with an equilibrium charge restoration driven by defects with reduced mobility. The full reversibility of the photo-potential in the case of MAPI/P and its irreversibility in the case of MAPI/T demonstrate the crucial role of the interfaces with charge-selective layers in ruling photochemistry of $MAPbI_3$ film. We suggest

that different photochemistry is activated in the two systems, as also suggested by the absence of PL recovery in the MAPI/T case, and that the films grown on TiO_2 may even undergo irreversible modifications.

Present results suggest that the MAPI/P stack is less prone to permanent degradation and might be more attractive than the MAPI/T stack for high irradiance applications.

Supporting Information
Supporting Information is available from the Wiley Online Library or from the author.

Acknowledgements
Authors declare no conflict of interest.
Research was not supported by specific funding.
A.T. S.M.P., G.I., V.S., M.Z. conceived the experiments. A.T., S.M.P. designed and implemented TR-SEM and PL customized setup. G.I., A.T., S.M.P. run the experiments. J.M.B. prepared the samples. G.I. S.M.P processed the experimental data. A.J.B. provided charge transport simulations. S.M.P., G.I., A.J.B., A.P. A.T., G.L. contributed to the interpretation of the results. S.M.P. took the lead in writing the manuscript, A.T. critically reviewed the manuscript. G.I. contributed to figure design. All authors provided critical feedback and helped in shaping the manuscript.
Authors thank Prof. Ermanno Pinotti for helpful discussion.

Received: ((will be filled in by the editorial staff))
Revised: ((will be filled in by the editorial staff))
Published online: ((will be filled in by the editorial staff))

References

[1] H. J. Snaith, *J. Phys. Chem. Lett.* **2013**, *4*, 3623.

[2] Y. Wu, F. Xie, H. Chen, X. Yang, H. Su, M. Cai, Z. Zhou, T. Noda, L. Han, *Adv. Mater.* **2017**, *29*, 1.

[3] J. M. Ball, A. Petrozza, *Nat. Energy* **2016**, *1*, 16149.

[4] F. Alta, E. S. Asu, *Www.Nrel.Gov* **2019**2020.

[5] T. Leijtens, S. D. Stranks, G. E. Eperon, R. Lindblad, E. M. J. Johansson, I. J. McPherson, H. Rensmo, J. M. Ball, M. M. Lee, H. J. Snaith, *ACS Nano* **2014**, *8*, 7147.

[6] A. Alnuaimi, I. Almansouri, A. Nayfeh, *AIP Adv.* **2016**, *6*, 115012.

[7] Z. Wang, Q. Lin, B. Wenger, M. G. Christoforo, Y. H. Lin, M. T. Klug, M. B. Johnston, L. M. Herz, H. J. Snaith, *Nat. Energy* **2018**, *3*, 855.

[8] Q. Lin, Z. Wang, H. J. Snaith, M. B. Johnston, L. M. Herz, *Adv. Sci.* **2018**, *5*, 1.

[9] S. D. Stranks, R. L. Z. Hoye, D. Di, R. H. Friend, F. Deschler, *Adv. Mater.* **2019**, *31*, 1803336.

[10] B. R. Sutherland, E. H. Sargent, *Nat. Photonics* **2016**, *10*, 295.

[11] E. Y. Tiguntseva, G. P. Zograf, F. E. Komissarenko, D. A. Zuev, A. A. Zakhidov, S. V. Makarov, Y. S. Kivshar, *Nano Lett.* **2018**, *18*, 1185.

[12] S. A. Veldhuis, P. P. Boix, N. Yantara, M. Li, T. C. Sum, N. Mathews, S. G. Mhaisalkar, *Adv. Mater.* **2016**, *28*, 6804.

[13] P. Lova, P. Giusto, F. Di Stasio, G. Manfredi, G. M. Paternò, D. Cortecchia, C. Soci, D. Comoretto, *Nanoscale* **2019**, *11*, 8978.

[14] M. Saba, M. Cadelano, D. Marongiu, F. Chen, V. Sarritzu, N. Sestu, C. Figus, M. Aresti, R. Piras, A. Geddo Lehmann, C. Cannas, A. Musinu, F. Quochi, A. Mura, G. Bongiovanni, *Nat. Commun.* **2014**, *5*, 5049.

[15] B. R. Sutherland, E. H. Sargent, *Nat. Photonics* **2016**, *10*, 295.

[16] G. Xing, N. Mathews, S. S. Lim, N. Yantara, X. Liu, D. Sabba, M. Grätzel, S. Mhaisalkar, T. C. Sum, *Nat. Mater.* **2014**, *13*, 476.

[17] Y. Li, X. Xu, C. Wang, B. Ecker, J. Yang, J. Huang, Y. Gao, *J. Phys. Chem. C* **2017**, *121*, 3904.

[18] R. K. Misra, S. Aharon, B. Li, D. Mogilyansky, I. Visoly-Fisher, L. Etgar, E. A. Katz, *J. Phys. Chem. Lett.* **2015**, *6*, 326.

[19] A. Alberti, E. Smecca, S. Sanzaro, G. Mannino, L. Deretzis, A. La Magna, *La Riv. Del Nuovo Cim.* **2019**, *42*, 301.

[20] I. Zarazua, J. Bisquert, G. Garcia-Belmonte, *J. Phys. Chem. Lett.* **2016**, *7*, 525.

[21] D. W. deQuilettes, W. Zhang, V. M. Burlakov, D. J. Graham, T. Leijtens, A. Osherov, V. Bulović, H. J. Snaith, D. S. Ginger, S. D. Stranks, *Nat. Commun.* **2016**, *7*, 11683.

[22] L. Kronik, Y. Shapira, *Surf. Interface Anal.* **2001**, *31*, 954.

[23] R. Gottesman, L. Gouda, S. Tirosh, A. Zaban, R. Gottesman, P. Lopez-varo, L. Gouda, J. A. Jimenez-tejada, J. Hu, *Chem* **2016**, *1*, 776.

[24] M. Daboczi, I. Hamilton, S. Xu, L. Joel, L. Saurav, L. Jinho, M. A. McLachlan, L. Kwanghee, J. R. Durrant, B. Iain, J. Kim, *ACS Appl. Mater. Interfaces* **2019**, *11*, 46808.

[25] J. R. Harwell, T. K. Baikie, I. D. Baikie, J. L. Payne, C. Ni, J. T. S. Irvine, G. A. Turnbull, I. D. W. Samuel, *Phys. Chem. Chem. Phys.* **2016**, *18*, 19738.

[26] V. W. Bergmann, S. A. L. Weber, F. Javier Ramos, M. K. Nazeeruddin, M. Grätzel, D. Li, A. L. Domanski, I. Lieberwirth, S. Ahmad, R. Berger, *Nat. Commun.* **2014**, *5*, 5001.

[27] L. Barnea Nehoshtan, S. Kirmayer, E. Edri, G. Hodes, D. Cahen, *J. Phys. Chem. Lett.* **2014**, *5*, 2408.

[28] G. Irde, S. M. Pietralunga, V. Sala, M. Zani, J. M. Ball, A. J. Barker, A. Petrozza, G. Lanzani, A. Tagliaferri, *Micron* **2019**, *121*, 53.

[29] J. Cazaux, *J. Electron Microsc. (Tokyo).* **2012**, *61*, 261.

[30] P. May, J. M. Halbout, G. Chiu, *Appl. Phys. Lett.* **1987**, *51*, 145.

[31] D.-S. Yang, O. F. Mohammed, A. H. Zewail, *Proc. Natl. Acad. Sci.* **2010**, *107*, 14993.

[32] J. Sun, A. Adhikari, B. S. Shaheen, H. Yang, O. F. Mohammed, *J. Phys. Chem. Lett.* **2016**, *7*, 985.

[33] M. Zani, V. Sala, G. Irde, S. M. Pietralunga, C. Manzoni, G. Cerullo, G. Lanzani, A. Tagliaferri, *Ultramicroscopy* **2018**, *187*, 93.

[34] S. G. Motti, M. Gandini, A. J. Barker, J. M. Ball, A. R. Srimath Kandada, A. Petrozza, *ACS Energy Lett.* **2016**, *1*, 726.

[35] S. G. Motti, D. Meggiolaro, A. J. Barker, E. Mosconi, C. A. R. Perini, J. M. Ball, M.

Gandini, M. Kim, F. De Angelis, A. Petrozza, *Nat. Photonics* **2019**, *13*, 532.

[36] S. G. Motti, D. Meggiolaro, S. Martani, R. Sorrentino, A. J. Barker, F. De Angelis, A. Petrozza, *Adv. Mater.* **2019**, *31*, 1901183.

[37] Z. Xiao, C. Bi, Y. Shao, Q. Dong, Q. Wang, Y. Yuan, C. Wang, Y. Gao, J. Huang, *Energy Environ. Sci.* **2014**, *7*, 2619.

[38] C. Tao, S. Neutzner, L. Colella, S. Marras, A. R. Srimath Kandada, M. Gandini, M. De Bastiani, G. Pace, L. Manna, M. Caironi, C. Bertarelli, A. Petrozza, *Energy Environ. Sci.* **2015**, *8*, 2365.

[39] K. W. A. Chee, C. Rodenburg, C. J. Humphreys, *J. Phys. Conf. Ser.* **2008**, *126*, 012033.

[40] J. Cazaux, *Ultramicroscopy* **2010**.

[41] H. Yuan, E. Debroye, K. Janssen, H. Naiki, C. Steuwe, G. Lu, M. Moris, E. Orgiu, H. Uji-I, F. De Schryver, P. Samorì, J. Hofkens, M. Roeffaers, *J. Phys. Chem. Lett.* **2016**, *7*, 561.

[42] A. R. Srimath Kandada, V. D'Innocenzo, G. Lanzani, A. Petrozza, in *Unconv. Thin Film Photovoltaics*, edited by F. De Angelis, A. Walker, E. Da Como, and H. Snaith (Royal Society of Chemistry, Cambridge, UK, 2016), pp. 107–140.

[43] L. Bertoluzzi, R. S. Sanchez, L. Liu, J. W. Lee, E. Mas-Marza, H. Han, N. G. Park, I. Mora-Sero, J. Bisquert, *Energy Environ. Sci.* **2015**, *8*, 910.

[44] M. N. Berberan-Santos, E. N. Bodunov, B. Valeur, *Chem. Phys.* **2005**, *315*, 171.

[45] K. C. Benny Lee, J. Siegel, S. E. D. Webb, S. Le´ veˆ que-Fort, M. J. Cole, R. Jones, K. Dowling, M. J. Lever, P. M. W. French, *Biophys. J.* **2001**, *81*, 1265.

[46] M. Berberan-Santos, E. N. Bodunov, B. Valeur, *Ann. Der Phys.* **2008**, *17*, 460.

[47] D. W. DeQuilettes, S. M. Vorpahl, S. D. Stranks, H. Nagaoka, G. E. Eperon, M. E. Ziffer, H. J. Snaith, D. S. Ginger, *Science (80-.).* **2015**, *348*, 683.

[48] A. Merdasa, M. Bag, Y. Tian, E. Källman, A. Dobrovolsky, I. G. Scheblykin, *J. Phys.*

Chem. C **2016**, *120*, 10711.

[49] R. Gottesman, L. Gouda, B. S. Kalanoor, E. Haltzi, S. Tirosh, E. Rosh-Hodesh, Y. Tischler, A. Zaban, C. Quarti, E. Mosconi, F. De Angelis, *J. Phys. Chem. Lett.* **2015**, *6*, 2332.

[50] J. Xing, Q. Wang, Q. Dong, Y. Yuan, Y. Fang, J. Huang, *Phys. Chem. Chem. Phys.* **2016**, *18*, 30484.

[51] C. C. Stoumpos, C. D. Malliakas, M. G. Kanatzidis, *Inorg. Chem.* **2013**, *52*, 9019.

[52] P. Schulz, E. Edri, S. Kirmayer, G. Hodes, D. Cahen, A. Kahn, *Energy Environ. Sci.* **2014**, *7*, 1377.

[53] E. M. Miller, Y. Zhao, C. C. Mercado, S. K. Saha, J. M. Luther, K. Zhu, V. Stevanović, C. L. Perkins, J. Van De Lagemaat, *Phys. Chem. Chem. Phys.* **2014**, *16*, 22122.

[54] A. Buin, P. Pietsch, J. Xu, O. Voznyy, A. H. Ip, R. Comin, E. H. Sargent, *Nano Lett.* **2014**, *14*, 6281.

[55] A. J. Barker, A. Sadhanala, F. Deschler, M. Gandini, S. P. Senanayak, P. M. Pearce, E. Mosconi, A. J. Pearson, Y. Wu, A. R. Srimath Kandada, T. Leijtens, F. De Angelis, S. E. Dutton, A. Petrozza, R. H. Friend, *ACS Energy Lett.* **2017**, *2*, 1416.

[56] L. A. Frolova, N. N. Dremova, P. A. Troshin, *Chem. Commun.* **2015**, *51*, 14917.

[57] Q. Wang, Y. Shao, H. Xie, L. Lyu, X. Liu, Y. Gao, J. Huang, *Appl. Phys. Lett.* **2014**, *105*, 3.

[58] W. J. Yin, T. Shi, Y. Yan, *Appl. Phys. Lett.* **2014**, *104*.

[59] G. Abdelmageed, C. Mackeen, K. Hellier, L. Jewell, L. Seymour, M. Tingwald, F. Bridges, J. Z. Zhang, S. Carter, *Sol. Energy Mater. Sol. Cells* **2018**, *174*, 566.

[60] Z. Xiao, Y. Yuan, Y. Shao, Q. Wang, Q. Dong, C. Bi, P. Sharma, A. Gruverman, J. Huang, *Nat. Mater.* **2015**, *14*, 193.

[61] C. S. Jiang, M. Yang, Y. Zhou, B. To, S. Nanayakkara, J. Luther, W. Zhou, J. J. Berry, J. Van De Lagemaat, N. P. Padture, K. Zhu, M. M. Al-Jassim, *2015 IEEE 42nd*

Photovolt. Spec. Conf. PVSC 2015 **2015**, *6*, 1.

[62] W. Zhang, S. Pathak, N. Sakai, T. Stergiopoulos, P. K. Nayak, N. K. Noel, A. A. Haghighirad, V. M. Burlakov, D. W. Dequilettes, A. Sadhanala, W. Li, L. Wang, D. S. Ginger, R. H. Friend, H. J. Snaith, *Nat. Commun.* **2015**, *6*, 1.

[63] A. M. Cowley, S. M. Sze, *J. Appl. Phys.* **1965**, *36*, 3212.

[64] Y. Zhao, C. Liang, H. Zhang, D. Li, D. Tian, G. Li, X. Jing, W. Zhang, W. Xiao, Q. Liu, F. Zhang, Z. He, *Energy Environ. Sci.* **2015**, *8*, 1256.

[65] Y. Deng, Z. Xiao, J. Huang, *Adv. Energy Mater.* **2015**, *5*, 1.

[66] P. Lopez-Varo, J. A. Jiménez-Tejada, M. García-Rosell, S. Ravishankar, G. Garcia-Belmonte, J. Bisquert, O. Almora, *Adv. Energy Mater.* **2018**, *8*, 1.

[67] M. De Bastiani, G. Dell'Erba, M. Gandini, V. D'Innocenzo, S. Neutzner, A. R. S. Kandada, G. Grancini, M. Binda, M. Prato, J. M. Ball, M. Caironi, A. Petrozza, *Adv. Energy Mater.* **2016**, *6*, 1.

[68] I. Suárez, E. J. Juárez-Pérez, J. Bisquert, I. Mora-Serõ, J. P. Martínez-Pastor, *Adv. Mater.* **2015**, *27*, 6157.

[69] J. M. Frost, K. T. Butler, A. Walsh, *APL Mater.* **2014**, *2*, 081506.

[70] J. M. Frost, K. T. Butler, F. Brivio, C. H. Hendon, M. Van Schilfgaarde, A. Walsh, *Nano Lett.* **2014**, *14*, 2584.

[71] M. Coll, A. Gomez, E. Mas-Marza, O. Almora, G. Garcia-Belmonte, M. Campoy-Quiles, J. Bisquert, *J. Phys. Chem. Lett.* **2015**, *6*, 1408.

[72] X. Y. Zhu, V. Podzorov, *J. Phys. Chem. Lett.* **2015**, *6*, 4758.

[73] C. G. Bischak, C. L. Hetherington, H. Wu, S. Aloni, D. F. Ogletree, D. T. Limmer, N. S. Ginsberg, *Nano Lett.* **2017**, *17*, 1028.

[74] C. G. Bischak, E. M. Sanehira, J. T. Precht, J. M. Luther, N. S. Ginsberg, *Nano Lett.* **2015**, *15*, 4799.

[75] Y. Zhao, A. M. Nardes, K. Zhu, *J. Phys. Chem. Lett.* **2014**, *5*, 490.

[76] J. Kim, S. Lee, J. H. Lee, K. Hong, *J. Phys. Chem. Lett.* **2014**, *5*, 1312.

[77] T. Leijtens, E. T. Hoke, G. Grancini, D. J. Slotcavage, G. E. Eperon, J. M. Ball, M. De Bastiani, A. R. Bowring, N. Martino, K. Wojciechowski, M. D. McGehee, H. J. Snaith, A. Petrozza, *Adv. Energy Mater.* **2015**, *5*, 1.

[78] C. Eames, J. M. Frost, P. R. F. Barnes, B. C. O. Regan, A. Walsh, M. S. Islam, *Nat. Commun.* **2015**, *6*, 7497.

[79] J. M. Azpiroz, E. Mosconi, J. Bisquert, F. De Angelis, *Energy Environ. Sci.* **2015**, *8*, 2118.

[80] X. Yang, X. Yan, W. Wang, X. Zhu, H. Li, W. Ma, C. X. Sheng, *Org. Electron. Physics, Mater. Appl.* **2016**, *34*, 79.

[81] W. Zhang, M. Saliba, D. T. Moore, S. K. Pathak, M. T. Hörantner, T. Stergiopoulos, S. D. Stranks, G. E. Eperon, J. A. Alexander-Webber, A. Abate, A. Sadhanala, S. Yao, Y. Chen, R. H. Friend, L. A. Estroff, U. Wiesner, H. J. Snaith, *Nat. Commun.* **2015**, *6*, 6142.

[82] R. Gottesman, E. Haltzi, L. Gouda, S. Tirosh, Y. Bouhadana, A. Zaban, E. Mosconi, F. De Angelis, *J. Phys. Chem. Lett.* **2014**, *5*, 2662.

[83] X. Wu, H. Yu, L. Li, F. Wang, H. Xu, N. Zhao, **2015**.

[84] W. Nie, J. Blancon, A. J. Neukirch, K. Appavoo, H. Tsai, M. Chhowalla, M. A. Alam, M. Y. Sfeir, C. Katan, J. Even, S. Tretiak, J. J. Crochet, G. Gupta, A. D. Mohite, *Nat. Commun.* **2016**, *7*, 1.

[85] Y. Yoon, D. Ha, I. J. Park, P. M. Haney, S. Lee, N. B. Zhitenev, *Nano Energy* **2018**, *48*, 543.

[86] X. Deng, X. Wen, J. Zheng, T. Young, C. F. J. Lau, J. Kim, M. Green, S. Huang, A. Ho-Baillie, *Nano Energy* **2018**, *46*, 356.

[87] D. W. de Quilettes, S. M. Vorpahl, S. D. Stranks, H. Nagaoka, G. E. Eperon, M. E. Ziffer, H. J. Snaith, D. S. Ginger, *Science (80-.).* **2015**, *348*, 683.

[88] D. Hong, Y. Zhou, S. Wan, X. Hu, D. Xie, Y. Tian, *ACS Photonics* **2018**, *5*, 2034.

[89] X. Wen, S. Huang, S. Chen, X. Deng, F. Huang, Y. B. Cheng, M. Green, A. Ho-Baillie, *Adv. Mater. Interfaces* **2016**, *3*, 1.

[90] S. Chen, X. Wen, S. Huang, F. Huang, Y.-B. Cheng, M. Green, A. Ho-Baillie, *Sol. RRL* **2017**, *1*, 1600001.

[91] E. T. Hoke, D. J. Slotcavage, E. R. Dohner, A. R. Bowring, H. I. Karunadasa, M. D. McGehee, *Chem. Sci.* **2015**, *6*, 613.

[92] A. Gomez, S. Sanchez, M. Campoy-Quiles, A. Abate, *Nano Energy* **2018**, *45*, 94.

[93] K. Wojciechowski, S. D. Stranks, A. Abate, G. Sadoughi, A. Sadhanala, N. Kopidakis, G. Rumbles, C. Z. Li, R. H. Friend, A. K. Y. Jen, H. J. Snaith, *ACS Nano* **2014**, *8*, 12701.

[94] H. W. Chen, N. Sakai, M. Ikegami, T. Miyasaka, *J. Phys. Chem. Lett.* **2015**, *6*, 164.

[95] A. Merdasa, Y. Tian, R. Camacho, A. Dobrovolsky, E. Debroye, E. L. Unger, J. Hofkens, V. Sundström, I. G. Scheblykin, *ACS Nano* **2017**, *11*, 5391.

[96] E. L. Unger, E. T. Hoke, C. D. Bailie, W. H. Nguyen, A. R. Bowring, T. Heumuller, M. G. Christoforod, M. D. McGehee, *Energy Environ. Sci.* **2014**, *7*, 3690.

[97] J. P. Correa Baena, L. Steier, W. Tress, M. Saliba, S. Neutzner, T. Matsui, F. Giordano, T. J. Jacobsson, A. R. Srimath Kandada, S. M. Zakeeruddin, A. Petrozza, A. Abate, M. K. Nazeeruddin, M. Grätzel, A. Hagfeldt, *Energy Environ. Sci.* **2015**, *8*, 2928.

[98] D. Wang, M. Wright, N. K. Elumalai, A. Uddin, *Sol. Energy Mater. Sol. Cells* **2016**, *147*, 255.

[99] W. Tress, N. Marinova, T. Moehl, S. M. Zakeeruddin, M. K. Nazeeruddin, M. Grätzel, *Energy Environ. Sci.* **2015**, *8*, 995.

[100] G. Murugadoss, S. Kanaya, T. Umeyama, H. Nishino, S. Ito, H. Imahori, S. Tanaka, G. Mizuta, S. Kanaya, H. Nishino, T. Umeyama, H. Imahori, S. Ito, *Jpn. J. Appl. Phys.* **2015**, *54*, 08KF08.

Figure 1. $MAPbI_3$ planar heterostructures: top view SEM images at surface and scheme of the cross sections. Images are taken under identical experimental conditions, so that higher brightness is an indication of higher efficiency in SE emission from the film. (i): the "standard" *n-i* stack (MAPI/T); (ii): the partial "inverted" *p-i* stack (MAPI/P). Fluorine-doped-tin-oxide (FTO) and Indium-doped-tin-oxide (ITO) transparent contacts are also shown

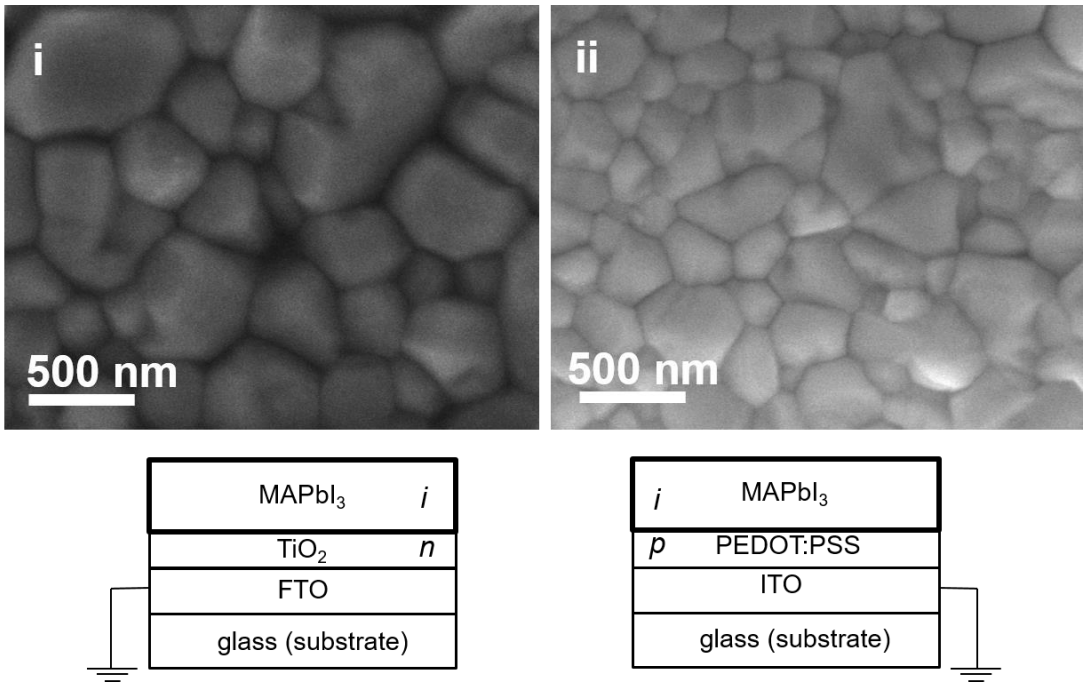

Figure 2. Time-Resolved SEM coupled with *in-situ* PL setup: (a): picture of the measurement chamber, showing the SEM column, the optical feedthrough for PL signal collection (on the right) and tilted $MAPbI_3$ sample illuminated by laser light (b): the scheme of the corresponding experimental configuration

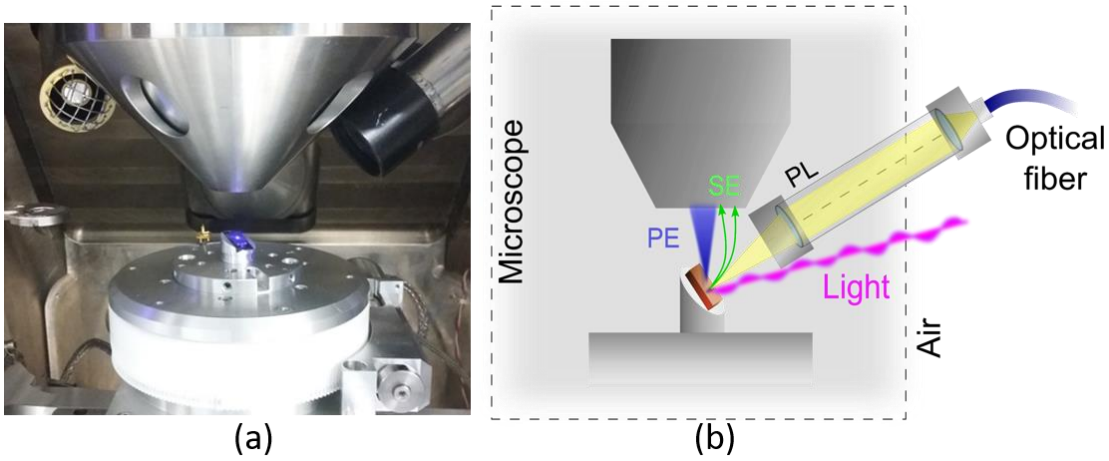

Figure 3. Comparison of dynamical light-induced TR-SEM images, during CW illumination at 405nm (Laser ON) and after switching illumination off (Laser OFF) for MAPI/P (first row) and MAPI/T (second row) films. (a): TR-SEM differential contrast maps taken after illuminating for 120s and after resting in dark for 120s. The dashed ellipse marks the laser spot, at grazing incidence. (b): evolution of contrast profiles extracted along the minor axis of the illuminated areas, as indicated by black arrows. Being the samples tilted, more negative positions correspond to surface points closer to the SEM column along its axis. (c): evolution of peak-to-peak contrast amplitudes, corresponding to profiles. [Contrast profiles for MAPI/P reproduced with permission [28], 2019, Elsevier., according to STM provisions].

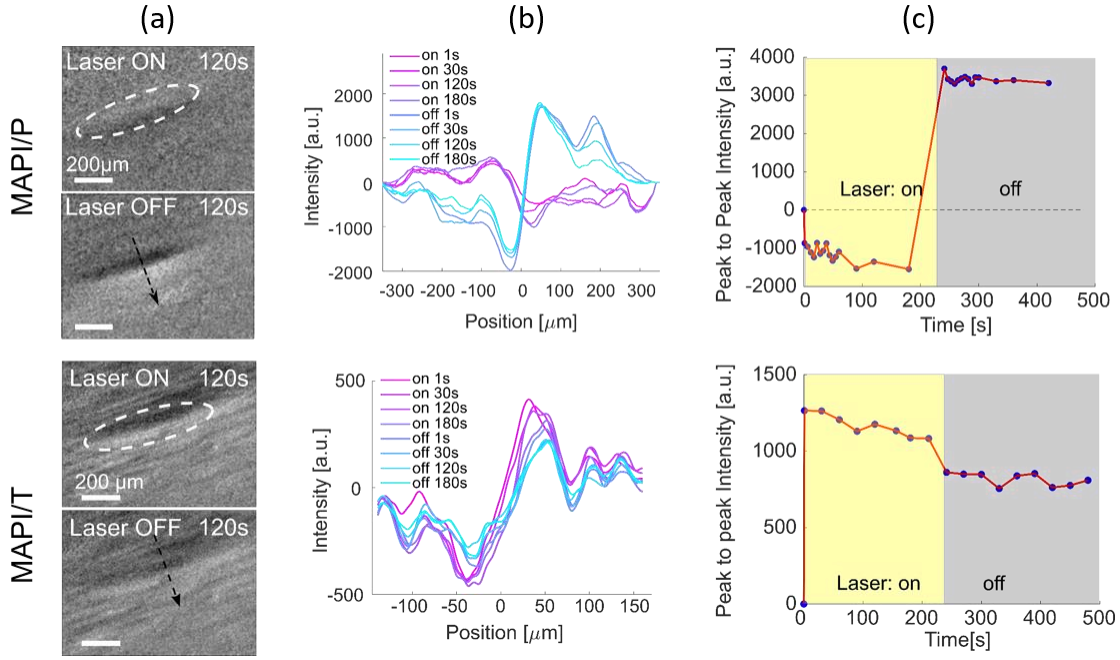

Figure 4. Comparison of functional shapes for experimentally measured and simulated TR-SEM contrast profiles. (a): selected experimental profiles taken across the minor axis of the illuminated elliptical regions and singled out from those in Figure 3, for both MAPI/T and MAPI/P samples, respectively in *Laser ON* (on) and *Laser OFF* (off). (b): numerically simulated SE contrast profiles (solid lines), and corresponding normal photovoltage distributions (dashed lines). Red curves: positive photovoltage values; green curves: negative photovoltage values.

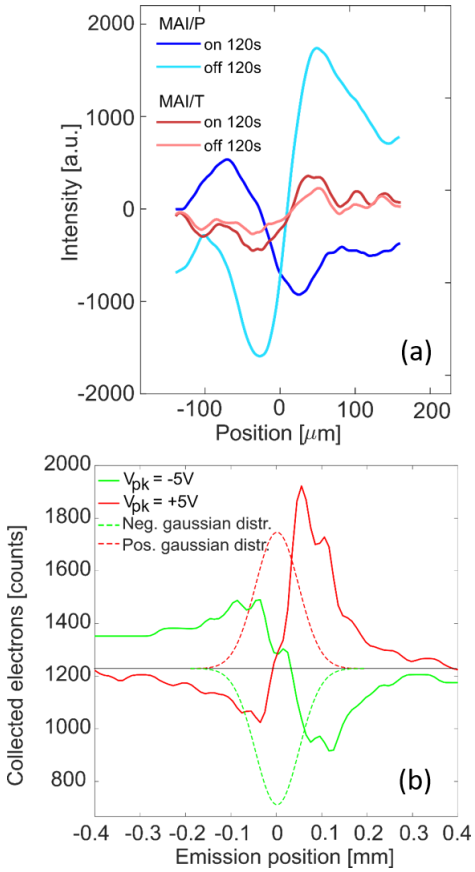

Figure 5. Optically induced modifications at the surface of MAPI/T sample, by SEM top-view images; (a): pristine area before optical irradiation; (b): the same area after being irradiated at 500 suns for 480 seconds and after 10 minutes of resting in the dark; (c): pixel-by-pixel differential contrast image; (d) white contours highlight modifications located at well defined crystalline grains.

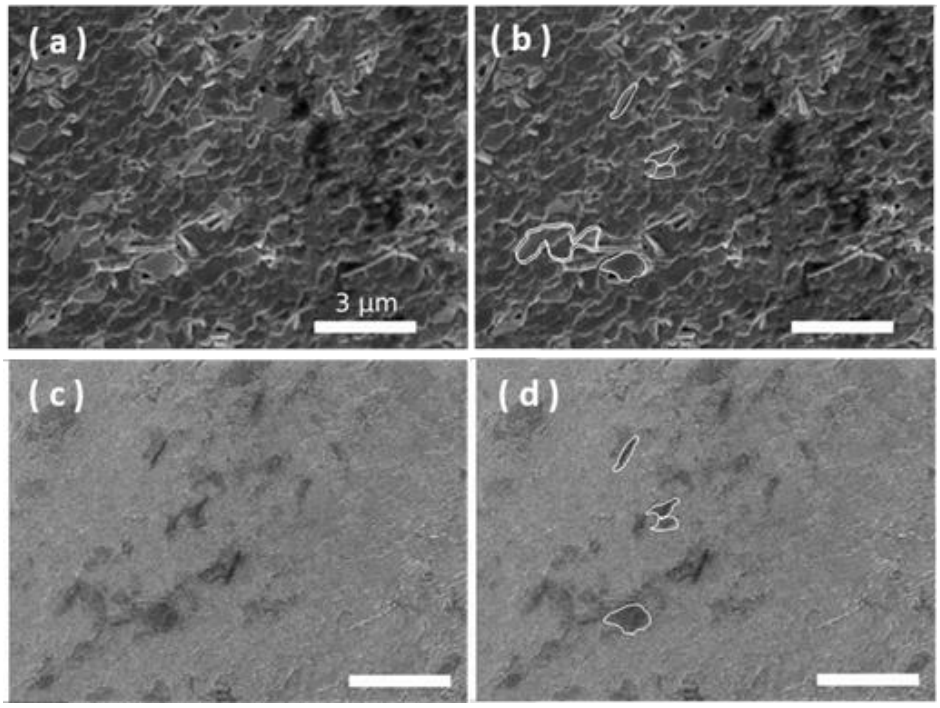

Figure 6. Figure 6: Temporal decay of spectrally integrated PL (a): Compared PL dynamics under illumination at 500 suns in MAPI/P and MAPI/T. Experimental data (points) are fitted with stretched exponential curves (solid lines). (b)-(d): Compared PL dynamics at 500 suns (b - MAPI/P, c - MAPI/T) and 15 suns (d - MAPI/P, e - MAPI/T), including the dark interval.

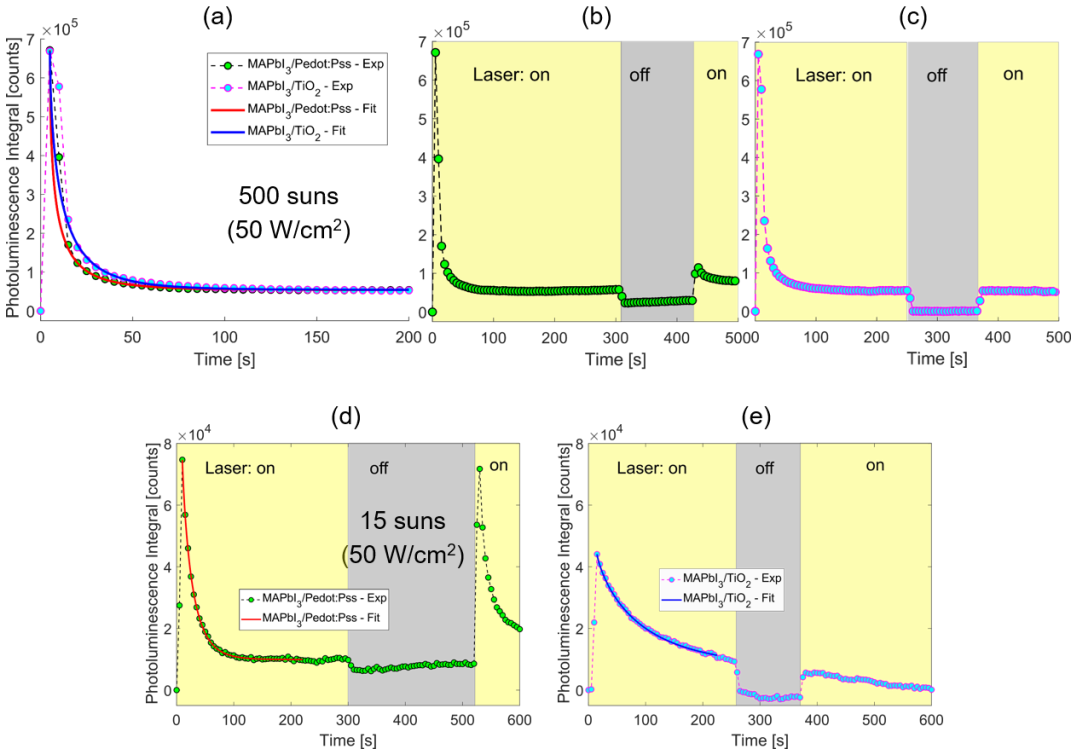

Figure 7. Energy diagrams of MAPI/T and MAPI/P systems at equilibrium in the dark. The excitation of hot SE by incident Primary Electron (PE) beam in SEM is indicated. a): in MAPI/T the condition $\Phi_T < \Phi_{MAPI} < \Phi_s$ leads to downward band bending at the ETL contact and upward bending at surface. Electrons (black dots) are collected at ETL, while a Coulomb force opposes to SE emission. b):in MAPI/P, the condition $\Phi_P > \Phi_{MAPI} > \Phi_s$ leads to upward band bending at the HTL contact and downward bending at surface. Electrons are accumulated at the HTL interface, while SE emission is eased. A slightly p-type character has been suggested for the $MAPbI_3$ film.

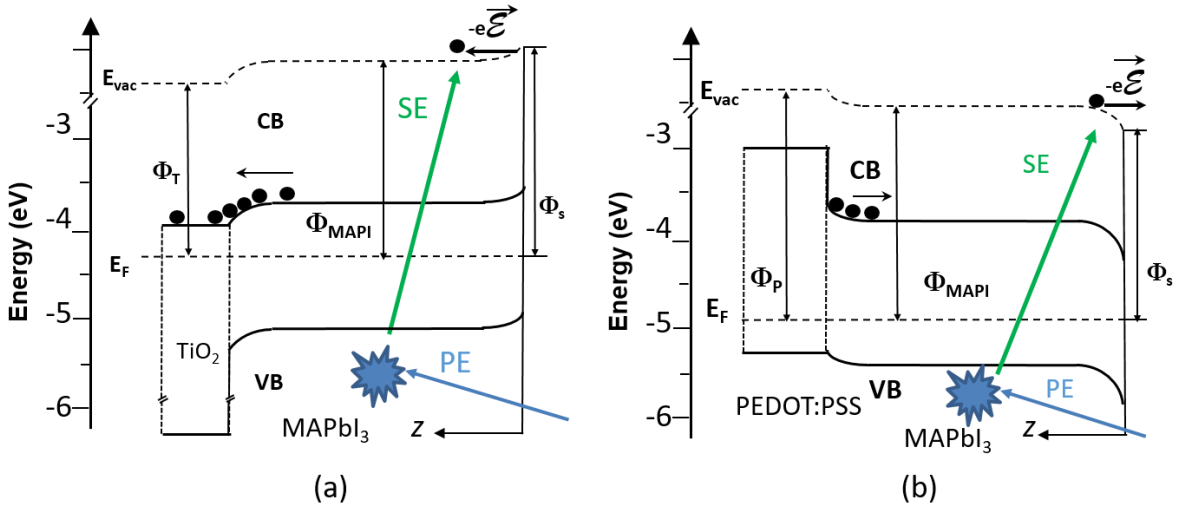

Figure 8. Evolution of the energy diagrams for MAPI/T system (top row) and for MAPI/P (bottom row) under CW high irradiance conditions at startup (a, d), after few 10 s (b,e) and during the recovery in dark (c,f). Black (white) dots represent electrons (holes). The blue line represents the illumination profile. The variations in dipole moment at surface are graphically indicated by $\Delta\Phi_s$, representing the work function difference between not-illuminated and illuminated surface regions. Quasi-equilibrium Fermi Level is drawn. Sections (a,d): energy band flattening at the free surface by optically excited e-h plasma and quenching of the local electrical field. Sections (b,e): light-assisted mixed ionic-electronic contribution to local polarization at surface of $MAPbI_3$ films. Under photo-excitation, intragap deep electron traps (black dots in well) are filled. Optically activated negatively charged point defects move and diffuse away from the surface until a bipolar space charge field builds up and quenches the migration. Sections (c,f): evolution in dark. After free charge recombination, the space charge field contributes a positive self-biasing $V_{pv}=-e\Delta\Phi_s$. Back-diffusion and drift of defects brings the systems back towards the initial condition of neutrality, which is finally attained only in MAPI/P.

Annex (red framed): under illumination and open-circuited, the MAPI/T (n-i) heterojunction is illuminated at the anode surface and the illuminated zone is at more positive potential than the surroundings; the MAPI/P (p-i) heterojunction is illuminated at the cathode surface and the illuminated zone is at more negative potential than the surroundings

.

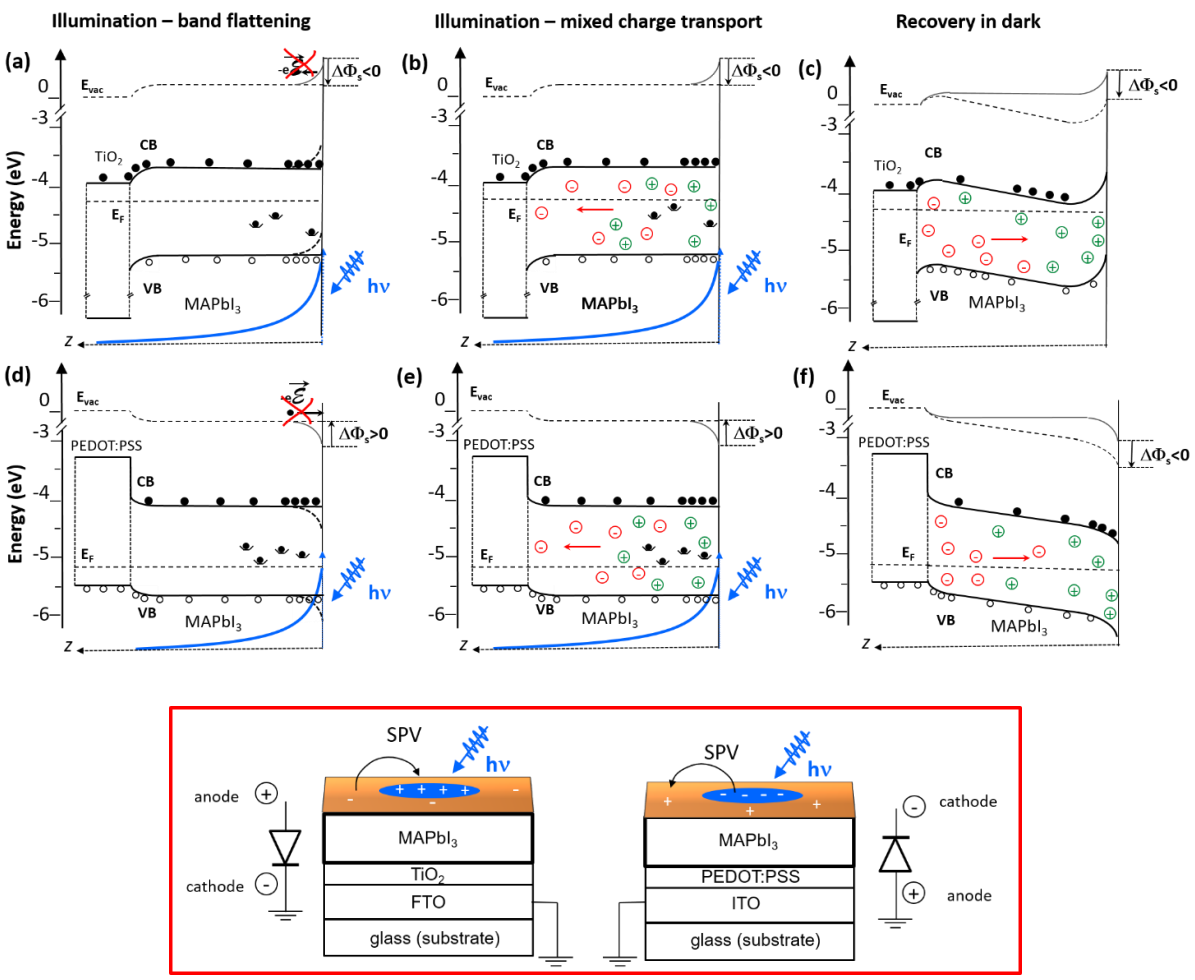

Table 1. Table 1: stretched exponential fitting parameters and averaged decay time for PLID.

	500 suns			15 suns		
System	**τ_c (s)**	**β**	**$<\tau>$ (s)**	**τ_c @ (s)**	**β**	**$<\tau>$ (s)**
$MAPbI_3$/PEDOT:PSS	3.41	0.52	6,23	17.86	0.88	19,09
$MAPbI_3/TiO_2$	6.71	0.63	9,47	78.92	0.81	88,30

ToC

Illumination of $MAPbI_3$ thin films at 500 suns may induce giant photo-potentials at the free film surface. Their recovery dynamics crucially depends on the nature of selective contact at substrate. TiO_2 contacts issue a permanent surface polarization effect, also suggesting a role of TiO_2 as a catalyst for photo-assisted redox reaction paths ultimately causing local degradation of the perovskite operated under high irradiance.

Keyword
Photovoltaic devices

Authors

Silvia Maria Pietralunga*, Gabriele Irde, Alex J Barker, James M. Ball, Annamaria Petrozza, Vittorio Sala, Maurizio Zani, Guglielmo Lanzani, Alberto Tagliaferri

*Silvia Maria Pietralunga, Corresponding Author

Title
Dynamical Imaging of Surface Photo-potentials in Hybrid Lead Iodide Perovskite Films under High Optical Irradiance and the Role of Selective Contacts

ToC figure (PNG) (55 mm broad × 50 mm high)

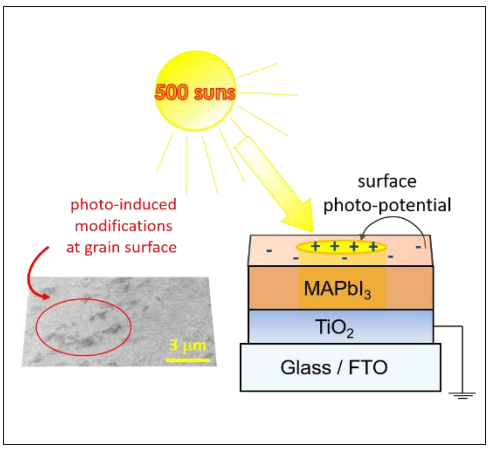

Supporting Information

Dynamical Imaging of Surface Photo-potentials in Hybrid Lead Iodide Perovskite Films under High Optical Irradiance and the Role of Selective Contacts

Silvia Maria Pietralunga, Gabriele Irde, Alex J Barker, James M. Ball, Annamaria Petrozza, Vittorio Sala, Maurizio Zani, Guglielmo Lanzani, Alberto Tagliaferri.*

**Silvia Maria Pietralunga, Corresponding Author*

$MAPbI_3$ samples

$MAPbI_3$ films have been deposited onto TCO-coated clean glass substrates by the two-step interdiffusion method [1]. Two different structures were fabricated. In the first case films are deposited on top of a fluorine-doped tin oxide (FTO)-coated glass substrate with an electron-selective contact interlayer (ETL, electron-transport-layer) made of compact TiO_2, resulting in a $MAPbI_3/TiO_2$/FTO stack, here named MAPI/T. In the second case, films are grown on an indium-tin-oxide (ITO)-coated glass substrate with a poly (3,4-ethylenedioxythiophene) polystyrene sulfonate (PEDOT:PSS) hole-selective contact (HTL, hole-transport-layer), in a $MAPbI_3$/PEDOT:PSS/ITO sequence, here named MAPI/P.

The substrates were first cleaned sequentially in 1 vol% Hellmanex III (Sigma-Aldrich) in de-ionised (DI) water, twice in DI water, then in isopropanol (IPA, Sigma-Aldrich), acetone (Sigma-Aldrich), and IPA again under ultrasonic agitation, followed by 6 minutes exposure to O_2 plasma. To fabricate part of an *inverted* perovskite solar cell structure [2], Indium-tin-oxide (ITO) coated substrates have been used and poly (3,4-ethylenedioxythiophene) polystyrene sulfonate (PEDOT:PSS) interlayer has been spin coated (speed = 4000 rpm, acceleration = 4000 rpm/s, time = 60s) on top of the ITO layer, from a dispersion (Heraeus AI 4083) filtered with a

0.45 um polyvinylidene fluoride (PVDF) filter, and then annealed in air at 120°C for 10 minutes. To fabricate part of a *standard* perovskite solar cell structure, Fluorine–doped Tin Oxide (FTO) have been used and an interlayer of compact TiO_2 film has been deposited by spin coating (speed = 2000 rpm, acceleration = 2000 rpm/s, time = 60s) from a solution containing 70 μl titanium-isopropoxide (Sigma-Aldrich) and 2.5 μl of 2M HCl (Sigma-Aldrich, 37%, diluted with DI water) per 1 ml of anhydrous IPA (Sigma-Aldrich), that was filtered with a 0.2 um polytetrafluoroethylene (PTFE) filter, followed by drying at 150C for 10 minutes and annealing at 500C for 30 minutes in air. The substrates were then immediately transferred to a nitrogen-filled glovebox. $MAPbI_3$ films were synthesized by first depositing a film of PbI_2 (Alfa Aesar, 99.9985%) on top of either PEDOT:PSS or TiO_2 by spin coating (speed = 6000 rpm, acceleration = 6000 rpm/s, time = 30s) from a hot (70°C) 500 mg/ml solution in dimethylformamide (DMF), and then heated up to 100°C for 5 minutes. After cooling to room temperature, methylammonium iodide (MAI, Dyesol, 98%) was then spin-coated (speed = 6000 rpm, acceleration = 6000 rpm/s, time = 30s) on top from a hot (70°C) 50 mg/ml solution in IPA. The coated substrates were then transferred on a hotplate into closed petri dish containing a 10 μl DMF droplet for solvent annealing at 100°C for 1 hour to finally crystallize the perovskite films.

Experimental Setup for TR-SEM and In-Situ PhotoLuminescence

TR-SEM relies on a customized commercial SEM (Mod. Tescan MIRA III) operating in High Vacuum at $5 \cdot 10^{-4} \div 5 \cdot 10^{-5}$Pa and provided with optical viewports to focus light at the surface of the sample under test. The technique has been recently presented [3].In this work, a setup for *in-situ* measurement of photoluminescence (PL) has been added to the experimental setup. Optical excitation to the sample under test is provided by deep blue light from a CW-

emitting diode laser at $\lambda = 405nm\ (3.06\ eV)$, focused at grazing incidence on the surface (incidence angle $\gamma \sim 70°$) over an area $\sim 2 \times 10^4 \mu m^2$. Intensity spans from 1.5 W/cm^2 to 50 W/cm^2, equivalent to 15 – 500 suns and corresponding to an incident photonic flux $10^{18} - 10^{20} photons/cm^2$. A refractive index value of n = 2.3 for the perovskite [4] gives a Fresnel reflectance coefficient $R = 0.35$ for incident light. An optical bandgap $E_g \cong 1.6$ eV, has been measured in $MAPbI_3$ films [3] and an absorption length $\alpha^{-1} \sim 140nm$ is estimated for blue light, where α (cm) is the absorption coefficient. When considering Lambert-Beer exponential absorption law, 85 - 90 % of light refracted into the perovskite film is absorbed over its thickness, while a non-negligible fraction (10-15%) of it reaches the selective contact layer at the bottom.

The sample is axially aligned with the electronic column and tilted by θ = 45° with respect to the vertical direction. Sample tilt provides the configurational asymmetry which is necessary to convey the information on photo-excited electrical phenomena [3]. Namely, sample tilting issues asymmetric bright-dark contrast patterns in the presence of localized charge distributions at surface. Pattern distribution also encode the information on the sign of the charge and of the resulting potentials, as explained in the following.

TR-SEM contrast patterns are derived by numerically processing of SEM images. Specifically, the average brightness signal is subtracted in all images to eliminate the possible contribution of scattered photons and to create a common contrast reference. Then the morphological contrast is cancelled by performing a pixel-by-pixel subtraction of a reference image of the sample, taken prior to illumination, from all the subsequent images. In this way the 2D contrast pattern is solely contributed by photoinduced phenomena. Experimentally observed dynamical SE patterns have been interpreted and related to the occurrence of photo-induced local surface potentials by numerical modelling of the process of SE emission and collection in the SEM under optical excitation, as detailed at length in the paper by Irde *et al.* [3].

In setting the experimental conditions, care was also taken to minimize electron-beam damaging of the $MAPbI_3$ films by choosing 5÷10 pA of current and 5keV of energy for the primary electrons (PE) [4,5]. Moreover, in this energy range the penetration depth of PEs is limited to the thickness of the $MAPbI_3$ film, as shown by Monte Carlo simulations of PE trajectories in the perovskite stack [3]. Therefore the underlying layers are not reached by the PE beam and e-beam probing of photo-induced potential entirely develops within the $MAPbI_3$ volume. Besides, under chosen SEM operating conditions (including magnification and speed of acquisition) the perturbation induced in the material by the electron beam is negligible with respect to the effects induced by the optical beam, in terms of energy deposited over the excitation volume and of excess charge carrier excitation.

In ordinary SEM imaging, SE contrast is contributed by sample morphology and by local work function values [6,7]. Under illumination, the work function can be modified by mechanisms such as photo-assisted chemical reactions, photo-excitation of electrical space charge fields and polar domains, up to phase transformations and morphological changes, the latter especially occurring at very high intense optical irradiation. All these phenomena affect the emission and collection of SEs [8] , leading to contrast patterns which can be imaged by TR-SEM. In the present case, optically induced morphological damage of the samples was avoided by keeping the optical intensity of the exciting laser far below an ascertained threshold [5].

The same laser source which excites TR-SEM patterns is also used to excite *in-situ* quasi–steady state PL at irradiance levels of 15 suns and 500 suns. The PL signal is collected by a custom optical fiber feedthrough, specifically devised to the purpose, and analyzed with a MAYA spectrometer (Ocean Optics) on the $250 \div 1100$ nm spectrum.

Spectra were acquired every 5 seconds (120 spectra over 10 minutes) with an integration time of 500 ms, and mediated over 10 acquisitions. The evolution of steady-state PL signal on long temporal scale was performed by exposing samples to laser light for 4-5 minutes, then by keeping them in the dark for 2-4 minutes and exposing them again to light for 4 additional

minutes to verify PL signal recovery. For PL measurements $MAPbI_3$ films were mounted at tilt angle $\theta = 45°$; by tuning the azimuthal angle ϕ, incidence angle for pumping laser light can vary between 50° and 80°.

TR-SEM: 2D mapping of surface electric field

In the formation of SEM images, a key role is played by the process of SE collection at the detector under the effects of electric and magnetic fields in the specimen chamber [9]. Also, the orientation of the surface of the specimen and the collection geometry crucially affect SE detection yield [9–11]. It may be stated that in the SEM the information is carried by existing asymmetries between the geometries of emission and detection of the SEs. In a fully symmetric SEM configuration, not even the well-known shadowing effects which carries the information on sample morphology would be generated [12].

In case of TR-SEM, a differential image post-processing routine eliminates the morphological contribution and the contrast is contributed by optically induced modifications in the material, which affect SE emission and collection. One of the most valuable information concerns static and dynamic local space charge segregation and optically induced polarization fields, that build-up as a consequence of optical absorption and which affect the potential distribution at surface. Therefore TR-SEM contrast patterns can be discussed in the frame of optically induced local photovoltaic effects at the surface of $MAPbI_3$ films.

On one side, the building up of localized space charge distribution in the specimen under analysis may affect the emission of SEs by modulating the energy barrier at surface through modulations in the work function. On the other side, the presence of an uneven potential distribution at surface also affects the vacuum space outside the specimen and close to it, by issuing *patch field*, which affect the trajectories of emitted SEs and their collection at the detector in dependence on their kinetic energy and emission point. All these effects must be

taken into consideration for a correct interpretation of the experimental results when using SEM to map local charge distributions [13,14]. Besides, a suitable asymmetric configuration must be devised, in order to carry the information on photo-excited surface potentials without any ambiguity.

In the TR-SEM setup here considered, an in-column SE detector is used, which implies a substantially axial detection symmetry. The asymmetry has been obtained by tilting the surface of the specimen under test with respect to the direction of the axis of the SEM column, as shown in Figure S1. The case here illustrated is referenced to the presence of a localized distribution of positive charge at the surface of the specimen. Emitted SE are channeled towards the detector by an accelerating field. If a charge unbalance is located at the sample surface, it issues an electric field distribution in the vacuum space in close proximity of the surface, that adds to the accelerating field and affects the overall electromagnetic configuration of the chamber. By numerically modelling the chamber configuration (in SIMION 8.0 software environment) it was demonstrated [3] that if a localized positive voltage distribution is present on a tilted specimen, SE emitted from the portion of the sample closer to the SEM column are less effectively collected than the SE emitted farther from the column. When accounting for the position from which SEs are emitted and by also weighting with the spectral distribution in kinetic energy of emitted electrons, the result is a dark-bright contrast pattern like the one pictured in Figure S1(a). Figure S1(b) plots the SE collection profiles taken across the charged zone as indicated. In case of positive potential, the collection is lower closer to the column and higher away from it. The opposite occurs in case of negative potential distribution.

This is the reference frame for interpreting localized potential distributions as the results of the optical excitation of charge dynamics in the material.

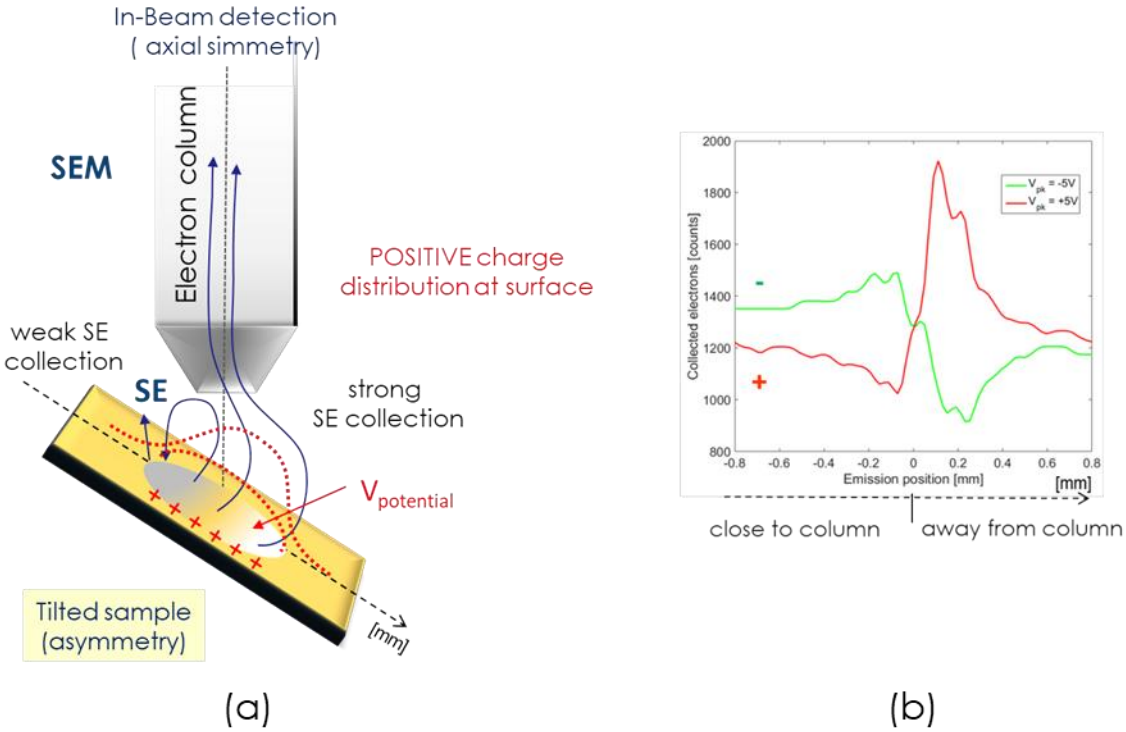

Figure S1: Formation of the dark-bright patterns in TR-SEM contrast. (a) asymmetric configuration in TR-SEM, featuring in-column detection, which is substantially symmetric with respect to the measurement chamber, and a tilted orientation for the sample under analysis. Symmetry-breaking carries the information. A localized positive charge distribution at surface generates an external electric field that sums to the accelerating field of the detector, leading to weaker SE collection close to the column and stronger collection away from the column. (b): Calculated cross profiles of the SE contrast along the direction shown in (a), in the case of localized surface voltage, normally distributed and with a peak amplitude of a few volts. Red and green lines correspond respectively to positive and negative voltage values.

TR-SEM : Temporal evolution of 2D contrast maps in Laser ON and Laser OFF conditions for MAPbI3 films on PEDOT:PSS and MAPbI3 films on TiO_2

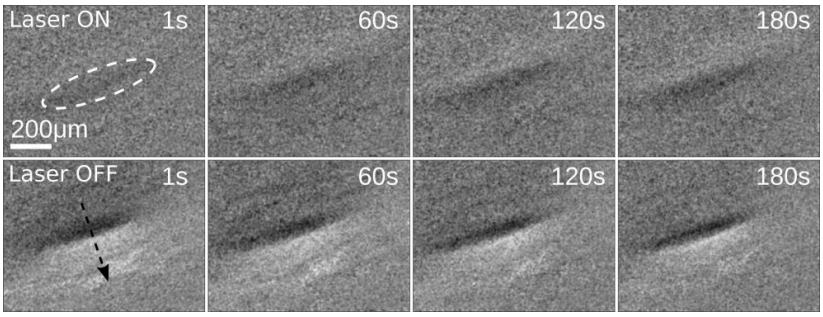

Figure S2: MAPbI3 films on PEDOT:PSS: 2D TR-SEM differential contrast maps. Temporal evolution of light induced TR-SEM images sampled along 180 s during cw illumination at 405nm (Laser ON) and then for 180s in the dark after illumination (Laser OFF). The dashed ellipse marks the position of the laser beam at grazing incidence with the sample.

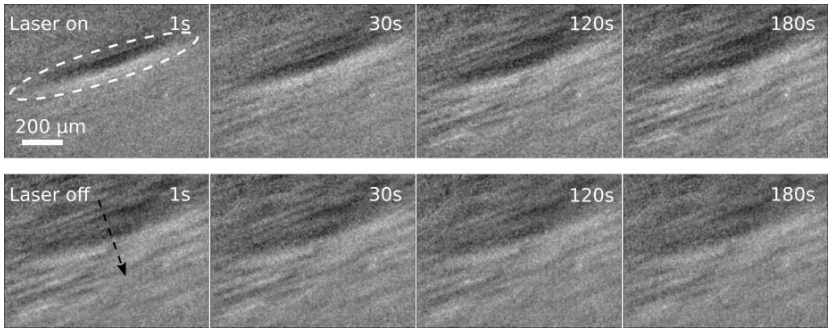

Figure S3: MAPbI3 films on TiO_2: 2D TR-SEM differential contrast maps. Temporal evolution of light induced TR-SEM images sampled along 180 s during cw illumination at 405nm (Laser ON) and then for 180s in the dark after illumination (Laser OFF). The dashed ellipse marks the position of the laser beam at grazing incidence with the sample.

TR-SEM: Long term decay of contrast in MAPI/P

The dependence of TR-SEM contrast on irradiating fluence is shown in Figure S4. Higher fluences correspond to longer permancences of the photoinduced contrast.

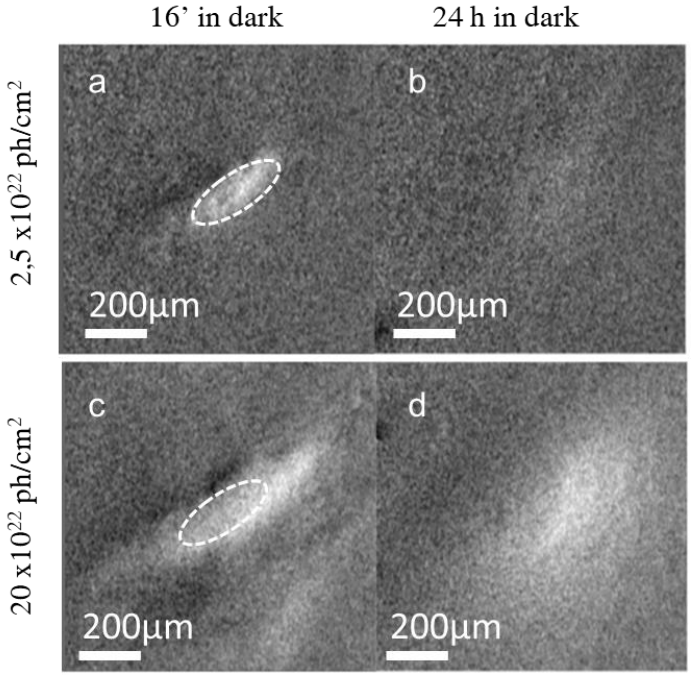

Figure S4: Dependence of the decay of TR-SEM contrast for the MAPI/P sample on the incident photon dose, i.e. integrated photon fluence in time. Frames (a) and (b) correspond to illuminating the sample for 2 minutes; frames (c) and (d) are obtained after illuminating the samples for 16 minutes.

As already shown by Irde et al. [3], when irradiating the film at 500 suns for 6 min, in MAPI/P pristine contrast conditions are substantially recovered after 10 min resting in the dark. At increased excitation fluences longer recovery times are necessary. For instance, TR-SEM patterns excited at 1000 suns for 16 minutes (corresponding to a fluence of $\sim 10^{22} ph\ cm^{-2}$) completely disappear after 3 days. In any case, by interpreting TR-SEM contrast as a photo-potential distribution, it can be stated that SPV induced by high optical irradiance in MAPI/P is a fully reversible phenomenon.

TR-SEM: Long term decay of contrast in MAPI/T

Figure S5 shows an example of long term evolution of TR-SEM contrast at the surface of a MAPI/T sample irradiated at 500 suns. The first frame on the left corresponds to the condition after 120s under illumination (Laser ON). Adjacent frames show the evolution of the contrast in the dark: from the condition immediately after turning illumination OFF (Laser OFF-1s), and then sampling the condition after 120s, 240s and 14 hours.

In the dark, the decay of the contrast tends to saturate on the time scale of minutes and a definite surface perturbation is still evident 14 hours after turning illumination off.

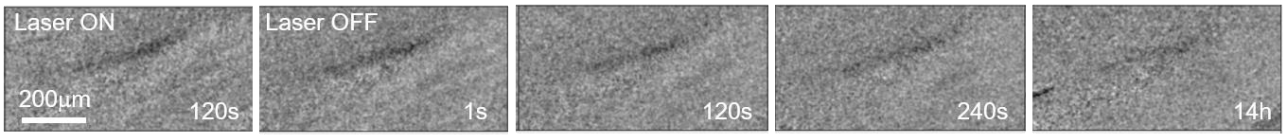

Figure S5: Long term decay of TR-SEM contrast for the MAPI/T sample. From left to right, the frames refer to the following conditions: after 120s under illumination (Laser ON), immediately after turning illumination OFF (Laser OFF-1s), resting in the dark for -respectively- 120s, 240s and 14 hours.

Photoluminescence decay

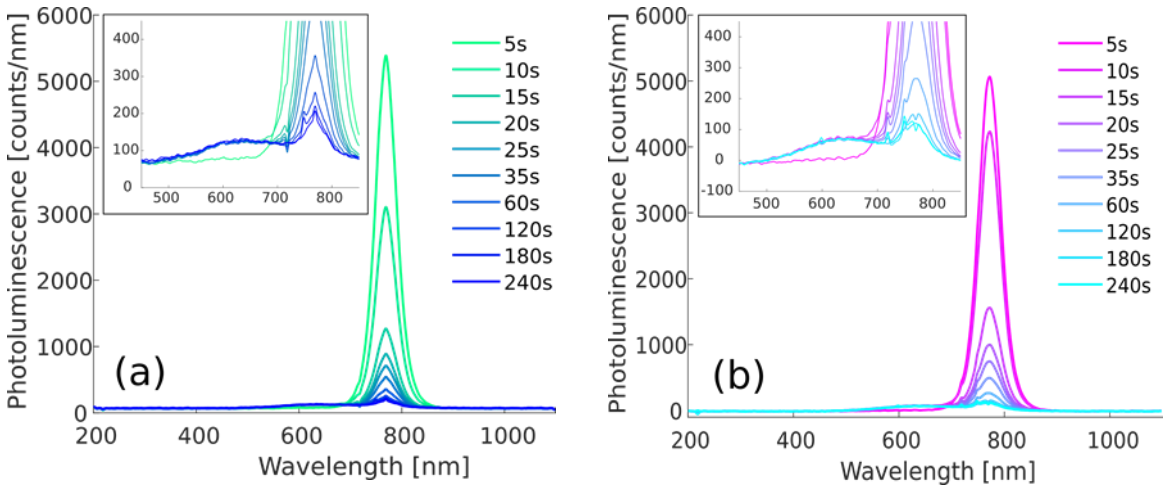

Figure S6: In-situ PL spectra taken at 500 suns (room temperature) on the MAPbI3 film, respectively grown on PEDOT:PSS (a) and on TiO_2 (b), showing a quenching of the main PL and the formation of an unquenched spectral shoulder at energies higher than the bandgap, detailed in the insets.

The time evolution of PL spectra, excited at irradiance of 500 suns equivalent, is shown in Figure S6 for both systems, at different illumination times. The reduction in spectrally integrated PLQY corresponds to a quenching of the main PL peak at 772 ± 2 nm (Kandada) over time. Quenching is already evident 5 seconds after switching illumination on and proceeds until PL emission saturates within a couple of minutes to a steady state at about 10% of its initial value. In both systems a broad PL shoulder at above bandgap energies ($\sim E_g + 0.37eV$) appears in about 10s after irradiation starts, which stays unquenched.

Figure S7 compares PL spectra, recorded in both systems after irradiating for 10s at either optical intensities. The inset is a zooming-in of the peak zone and highlights the formation of

the shoulder only when irradiating at 500 suns, suggesting that very high photon intensities are required to activate the phenomenon.

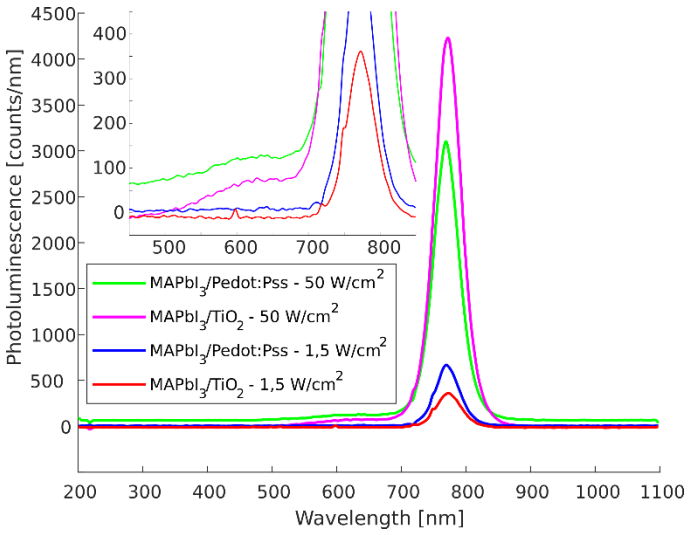

Figure S7: Comparison of PL spectra acquired on both systems 10 seconds after turning illumination on, at 500 suns and 15 suns. The spectral shoulder is absent at lower irradiance. The inset is a zoom of the peak zone, showing that the spectral shoulder is generated only at higher excitation intensity.

According to its temporal evolution and spectral shape, this broadening in PL spectrum cannot be justified as a band-filling effect of a Burstein-Moss kind (Manser) and its emergence may indicate some kind of photo-induced material modification. Photoinduced lattice instabilities at optical intensities of 100 suns (generation of I^- vacancies, but also of MA^+ vacancies and Pb^{2+} vacancies at highest irradiances) were reported, which may induce rearrangements and distortion in the inorganic Pb-I cage of the $MAPbI_3$ structure (/Gottesmann 2015, Merdasa). In turn, distortions in the Pb-I-Pb bond angle have been related to bandgap widening (Aspiroz). The occurrence of definite quenching and spectral shifts of the main PL peak under intense irradiation have been discovered and investigated by Merdasa and co-workers on single $MAPbI_3$ nanocrystals; they related this spectral dynamics to photoinduced degradation of the perovskite and segregation of PbI_2 clusters [15]. In our case, PL emission at energies higher than

the main PL peak may proceed from an overall bandgap widening contributed by diverse light-induced physical-chemical modifications at the molecular level.

[1] Z. Xiao, C. Bi, Y. Shao, Q. Dong, Q. Wang, Y. Yuan, C. Wang, Y. Gao, J. Huang, *Energy Environ. Sci.* **2014**, *7*, 2619.

[2] H. J. Snaith, *J. Phys. Chem. Lett.* **2013**, *4*, 3623.

[3] G. Irde, S. M. Pietralunga, V. Sala, M. Zani, J. M. Ball, A. J. Barker, A. Petrozza, G. Lanzani, A. Tagliaferri, *Micron* **2019**, *121*, 53.

[4] P. Loeper, M. Stuckelberger, B. Niesen, J. Werner, M. Filipic, S.-J. Moon, J.-H. Yum, M. Topic, S. De Wolf, C. Ballif, *J. Phys. Chem. Lett.* **2015**, *6*, 66.

[5] H. Yuan, E. Debroye, K. Janssen, H. Naiki, C. Steuwe, G. Lu, M. Moris, E. Orgiu, H. Uji-I, F. De Schryver, P. Samorì, J. Hofkens, M. Roeffaers, *J. Phys. Chem. Lett.* **2016**, *7*, 561.

[6] K. W. A. Chee, C. Rodenburg, C. J. Humphreys, *J. Phys. Conf. Ser.* **2008**, *126*, 012033.

[7] H. Seiler, *J. Appl. Phys.* **1983**, *54*, R1.

[8] J. Cazaux, *J. Electron Spectros. Relat. Phenomena* **2010**, *176*, 58.

[9] I. Müllerová, I. Konvalina, *J. Microsc.* **2009**, *236*, 203.

[10] J. Cazaux, *Ultramicroscopy* **2010**, *110*, 242.

[11] I. Konvalina, I. Müllerová, *Scanning* **2006**, *28*, 245.

[12] L. Reimer, *Scanning Electron Microscopy Physics of Image Formation and Microanalysis* (Springer-Verlag Berlin Heidelberg, 1985).

[13] J. Cazaux, *Ultramicroscopy* **2008**, *108*, 1645.

[14] J. Cazaux, *Scanning* **2004**, *26*, 181.

[15] A. Merdasa, M. Bag, Y. Tian, E. Källman, A. Dobrovolsky, I. G. Scheblykin, *J. Phys. Chem. C* **2016**, *120*, 10711.